

Title

Lee. R. Patrick



Doctor of Philosophy
The University of Edinburgh
Month Year

Abstract

Using a new spectroscopic technique to derive stellar parameters from Red Supergiants we derive stellar parameters for RSGs in NGC6822. With current state of the art KMOS instrument on the VLT, Chile, stellar parameters from red Supergiants can be probed at distances of up to ~ 5 Mpc. With a similar instrument operating on the E-ELT, this technique is feasible out to the Virgo cluster.

A new implementation of this technique is presented and tested on galaxies within the local group.

Using KMOS stellar parameters have been derived in NGC6822 at 0.5Mpc which represents the lowest metallicity environment this technique has been used on to date. These results agree well with previous estimates of metallicity using the young stellar population of this galaxy. There appears to be no significant metallicity gradient within this galaxy and the idea that Red Supergiant temperatures do not vary with metallicity is introduced.

At a greater distance, 20 RSGs in NGC 55 (2.2Mpc) are studied. This new technique is implemented and tested on Red supergiants at further distances in the galaxy NGC55. This represents the largest distance at which individual Red Supergiant stars have been studied in this great detail.

The selection of Red Supergiants using near-infrared photometry is investigated and developed by studying a large data set of red stars in the local group galaxy M33.

Declaration

I declare that this thesis was composed by myself, that the work contained herein is my own except where explicitly stated otherwise in the text, and that this work has not been submitted for any other degree or professional qualification except as specified.

Parts of this work have been published in ?.

(Lee. R. Patrick, Month Year)

Acknowledgements

I would like to thank myself for getting all of this work done ...

Contents

Abstract	i
Declaration	ii
Acknowledgements	iii
Contents	iv
List of Figures	vii
List of Tables	x
1 Introduction	1
1.1 The Life of a Red Supergiant	3
1.1.1 Birth	4
1.1.2 The Circle of Life	6
1.1.3 Death	10
1.2 Chemical Properties of Red Supergiants	12
1.2.1 <i>J</i> -band Analysis Technique	12
1.2.2 Galactic and Extragalactic RSGs	12
1.3 Chemical Evolution of Galaxies	16

2	J-band Sythentic Spectral Fitting	18
2.0.1	Continuum Fitting.....	18
2.0.2	Best Fit Parameters	20
3	Near-IR selection of Red Supergiants	24
4	KMOS Observations in NGC 6822	25
4.1	Introduction	25
4.2	Observations.....	27
4.2.1	Target Selection	27
4.2.2	KMOS Observations.....	28
4.3	Data Reduction	31
4.3.1	KMOS/esorex pipeline.....	31
4.3.2	Sky Subtraction	31
4.3.3	Telluric Correction.....	33
4.3.4	Three-arm vs 24-arm Telluric Correction.....	34
4.3.5	Telluric Correction Implementation.....	36
4.3.6	MOLECFIT	36
4.3.7	Stellar Radial Velocities	39
4.4	Results	40
4.4.1	Telluric Comparison	41
4.4.2	Stellar Parameters and Metallicity.....	41
4.5	Discussion	43
4.5.1	Metallicity Measurements	43
4.5.2	Temperatures of RSGs.....	47

4.5.3	AGB Contamination	49
4.6	Conclusions	49
5	Red Supergiants in NGC 55	54
A	The First Appendix	55
	Bibliography	57

List of Figures

(1.1) Hertzsprung–Russel diagram displaying evolutionary tracks of stars in the mass range $0.8 < M/M_{\odot} < 120$ taken from ?	6
(1.2) The evolutionary diversity of the end points of massive stars and their associated observed SN classification. Figure reproduced from ?. Acronym definitions: RSG, red supergiant; BSG, blue supergiant; LBV, luminous blue variable; WR, Wolf–Rayet; NS, neutron star; BH, black hole; GRB, gamma-ray burst; PISN, pair-instability supernova.	11
(1.3) Optical colour-magnitude diagram (CMD) of NGC 6822, in which the absolute V-band magnitude M_V , (corrected to the distance of NGC 6822) is plotted against B–V colour. This figure illustrates how CMDs can be used to separate stars based on spectral type. Redder colours indicate later spectral types. This figure also demonstrates that CMDs have inherent degeneracies between different populations of stars: the central dense feature at $B-V \sim 1.0$ is attributed to foreground contaminants.	15
(1.4) Optical colour–colour diagram of NGC 6822. This figure illustrates the surface gravity dependence of the B–V colour at a given V–R colour. The population with the redder B–V colours contain the RSG objects.	15
(2.1) Models at different resolutions.	19
(2.2) Illustration of the continuum width (cw) and slicing the model spectrum into regions of $cw\mu m$ is able to remove structure in order to fit the continuum. The solid black line shows an example of a model spectrum degraded to a resolution of 3000, blue points show the boundaries between the slices and red points show the maximum of each slice. Make this figure match Figure 2.1.	20

(4.1) Two-colour diagram for stars with good detections in the optical and near-IR photometry in NGC 6822. The black dashed line marks the selection criteria using optical colours, as defined by Levesque & Massey (2012). Red circles mark all stars which satisfied our selection criteria. Large blue stars denote targets observed with KMOS. The solid black line marks the foreground reddening vector for $E(B - V) = 0.22$ (Schlegel, Finkbeiner & Davis, 1998).	28
(4.2) Near-IR colour-magnitude diagram (CMD) for stars classified as stellar sources in the optical and near-IR catalogues, plotted using the same symbols as Figure 4.1. This CMD is used to supplement the optical selection. The solid black line marks the foreground reddening vector for $E(B - V) = 0.22$ (Schlegel, Finkbeiner & Davis, 1998).	29
(4.3) Spatial extent of the KMOS targets over a Digital Sky Survey (DSS) image of NGC 6822. Blue filled circles indicate the locations of the observed red supergiant stars. Red open circles indicate the positions of red supergiant candidates selected using out photometric criteria (see Section 4.2.1).	29
(4.4) IFU Snapshot	33
(4.5) Comparison of J -band spectra of the same standard star in each IFU. The ratio of each spectrum compared to that from the IFU used in the three-arm telluric method is shown, with their respective mean and standard deviation (μ and σ). Red lines indicate $\mu = 1.0$, $\sigma = 0.0$ for each ratio. The blue shaded area signifies the region used in our analysis, within which, the discrepancies between the IFUs are generally small. This is reflected in the standard deviation values when only considering this region. (IFUs 13 and 16 are omitted as no data were taken with these IFUs.)	35
(4.6) KMOS spectra of the NGC 6822 RSGs and their associated best-fit model spectra (black and red lines, respectively). The lines used for the analysis from left-to-right by species are: Fe I $\lambda\lambda 1.188285, 1.197305$, Si I $\lambda\lambda 1.198419, 1.199157, 1.203151, 1.210353$, Ti I $\lambda\lambda 1.189289, 1.194954$. The two strong Mg I lines are also labelled, but are not used in the fits (see Section 4.4).	37
(4.7) Radial velocities of targets shown against their distance from the galaxy centre. The average radial velocity for the sample is $-68 \pm 12 \text{ km s}^{-1}$. The green dashed line indicates H I systemic velocity ($-57 \pm 2 \text{ km s}^{-1}$; Koribalski et al., 2004). The radial velocities of two A-type supergiants from Venn et al. (2001) are shown in blue.	40

- (4.8) Comparison of the model parameters using the two different telluric methods. In each panel, the x-axis represents stellar parameters derived using the 3-arm telluric method and the y-axis represents those derived using the 24-arm telluric method. Top left: metallicity ($[Z]$), mean difference $\langle \Delta[Z] \rangle = 0.04 \pm 0.07$. Top right: effective temperature (T_{eff}), mean difference $\langle \Delta T_{\text{eff}} \rangle = -14 \pm 42$. Bottom left: surface gravity ($\log g$), mean difference $\langle \Delta \log g \rangle = -0.06 \pm 0.12$. Bottom right: Microturbulence (ξ), mean difference $\langle \Delta \xi \rangle = -0.1 \pm 0.1$. In all cases, the distributions are statistically consistent with a one-to-one ratio (black lines). 42
- (4.9) Derived metallicities for 11 RSGs in NGC 6822 shown against their distance from the galaxy centre; the average metallicity is $\bar{Z} = -0.52 \pm 0.21$. Blue and red points show blue supergiants results from Venn et al. (2001) and Muschelok et al. (1999) respectively. A least-squares fit to the KMOS results reveals a low-significance abundance gradient (see text for details). For comparison, $R_{25} = 460$ ($= 1.03$ kpc; McConnachie, 2012). 44
- (4.10) H-R diagram for the 11 RSGs in NGC 6822. Evolutionary tracks including rotation ($v/v_c = 0.4$) for SMC-like metallicity ($Z = 0.002$) are shown in grey, along with their zero-age mass (Georgy et al., 2013). Bolometric corrections are computed using the calibration in Davies et al. (2013a). We note that compared to the evolutionary tracks, the observed temperatures of NGC 6822 RSGs are systematically cooler. This is discussed in Section 4.5.2. 44
- (4.11) Effective temperatures as a function of metallicity for four different data sets using the J -band analysis technique. There appears to be no significant variation in the temperatures of RSGs over a range of 0.55 dex. These results are compiled from the LMC, SMC (blue and red points respectively; ?), PerOB1 (a Galactic RSG cluster; cyan; Gazak et al., 2014b) and NGC 6822 (green). Mean values for each data set are shown as enlarged points in the same style and colour. The x-axis is reversed for comparison with Figure 4.12. . 48
- (4.12) H-R diagram for RSGs in PerOB1 (cyan), LMC (blue), SMC (red) and NGC 6822 (green) which have stellar parameters obtained using the J -band method. This figure shows that there appears to be no significant temperature differences between the four samples. Solid grey lines show SMC-like metallicity evolutionary models including rotation (Georgy et al., 2013). Dashed grey lines show solar metallicity evolutionary models including rotation (Ekström et al., 2012). 48

List of Tables

(4.1) Measured velocity resolution and resolving power across each detector.	30
(4.2) Summary of VLT-KMOS targets in NGC 6822.	30
(4.3) c -values	38
(4.4) Model grid used for analysis.	41
(4.5) Fit parameters for reductions using the two different telluric methods.	41

Chapter 1

Introduction

Something witty and clever about RSGs and their environment!

Red supergiant (RSG) stars are massive, bright, evolved stars located exclusively in star-forming galaxies. The RSG phase of stellar evolution is thought to be passed through when a star begins its hydrogen-burning lifetime with an initial mass of $8 < M/M_{\odot} < 40$ (???). For massive stars, the hydrogen-burning lifetime of a star is short. This means that, although RSG stars are in an evolved state, they are in actual fact still remarkably young stellar objects (< 30 Myrs old). Given the fact that these stars are very young, in general they have not had the time to travel a significant distance from their birth place. Therefore, their chemical composition must closely match that of their surrounding environment (accounting sufficiently for a certain amount of nuclear processing).

In order to measure the chemical composition of these stars, and hence their surrounding environments, we must obtain spectroscopic observations. Typically, abundance measurements obtained from RSGs observations require high-resolution spectroscopy ($R \geq 20\,000$; ???). However, ? outline a method which uses low-resolution spectroscopy ($R \sim 3000$) at near infra-red (NIR) wavelengths to measure abundances. This is important as this PhD project intends to study the spectra of RSGs at Mpc distances in order to derive properties of their host galaxies, where high-resolution spectroscopy becomes unfeasible.

There are many reasons to study RSG stars at NIR wavelengths. From a technological point of view, the next generation of optical–infrared telescope (e.g. European Extremely Large Telescope, Thirty Metre Telescope, James Webb

Space Telescope) will be optimised for studies in the NIR; therefore, in order to make the best use of these facilities in the future, we must refine and optimise our observational strategy on facilities today. During this project this will be done by using the new K-band Multi-Object Spectrograph (KMOS), currently being commissioned on the Very Large Telescope, Chile.

There are also many intrinsic properties of RSGs which make them desirable objects to study in the NIR. Perhaps the property which illustrates this most efficiently is the fact that RSGs are very luminous in the NIR. So luminous in fact, that in the NIR, their luminosities can rival that of a small galaxy (?). This factor alone makes these objects good candidates to study at large distances. Coupled with this is the fact that NIR observations are less affected by dust obscuration. This is important in the context of RSGs as, by definition, RSGs are dusty objects, due to their high mass-loss rates (e.g. ?). Therefore, NIR observations are the optimal wavelength to observe RSG stars at large distances.

The study of RSGs in external galaxies provides important scientific insights in the study of fundamental stellar parameters as well as the chemical evolution of galaxies at large distances. Currently, the chemical composition of galaxies is measured using emission lines from large ionised hydrogen regions (HII regions). However, this method is highly dependent upon the chosen calibration (e.g. ?). Using RSG stars as abundance probes would provide an independent test of chemical composition which would then be used to calibrate observations at larger distances. Additional results include the study of various environmental factors affecting RSG evolution and the evolution of host galaxies, such as their nature and number, how chemical composition affects their evolution and the spatial distribution of RSGs in external galaxies. This will be made possible through the study of RSGs in a range of different galaxies, each with different individual characteristics.

The classification of stars is based on the morphology of their spectra, with particular focus upon the absorption lines of hydrogen and other elemental features such as helium and calcium. RSG stars have spectral type K or M, classified as such based on the appearance of strong molecular lines arising from their cool atmospheres. Additionally, cool main sequence dwarfs and evolved giant stars also have spectral type K or M. To distinguish between these populations of stars, luminosity is taken into account. For a given spectral type, the effective temperature is, to first approximation, constant, therefore, luminosity is dependent solely upon the radius of the star. The largest and most

luminous stars, the supergiants, are labelled as class I, giants as class III and dwarf stars, with the smallest radii and hence the lowest luminosity, as class V.

In general, spectral features which probe luminosity are directly related to the physical size of the star rather than a product of the luminosity. A star with a large physical size will have a small surface gravity, as surface gravity is inversely proportional to the square of the radius. RSGs have large extended atmospheres; hence, the surface gravity is considerably lower than the more compact dwarfs and giants. The low surface gravity of the supergiants produces various distinctive spectral features which are used to determine luminosity class. In the optical regime, there are various different luminosity class indicators. For K-type stars, the ratio of the YII (4376Å) line with FeI (4383Å) or the morphology of the CaII H and K lines (for early K-type stars) are some of the most prominent (?). While for M-type stars, a system of molecular TiO lines centred on 5000Å or the negative luminosity effect of the CaI (4226Å) line are clear indicators of luminosity (?). In the infrared, the 0-0 band of the CN molecule is the main luminosity discriminator at $\sim 1.1\mu\text{m}$ for both K- and M-type stars (?).

Distinguishing between dwarfs, giants and supergiants for a given spectral type is important as these stars are different in terms of their stage of evolution and mass. RSG stars are young, evolved stars that start their lives as stars with masses of $8 < M/M_{\odot} < 40$ and are fusing helium in their cores. In contrast, dwarf M- and K-type stars are low mass, old stars which are still in the core hydrogen fusion stage. Giant M- and K-type stars are evolved stars of intermediate mass and intermediate age currently on the asymptotic giant branch (AGB). The exact divide between AGB stars and RSGs stars is, like all classification sequences which attempt to bin a continuous range of data, somewhat ambiguous. Therefore, it is useful to outline the history and evolution of RSG stars and, in particular, what evolutionary factors make these stars unique.

1.1 The Life of a Red Supergiant

Stellar evolution is critically dependent upon the initial mass of the star. A $10M_{\odot}$ star has a very different evolutionary path to that of a solar mass star. Their formation, subsequent evolution and eventual fate all depend upon how much mass the star is able to accumulate during its formation. Therefore, an understanding of how massive stars are able to gather their mass in the first

place is crucial to the understanding of how these objects evolve and end their lives. To this end, this section is arranged into the following sections: Section ?? provides a brief outline of the main processes by which star formation occurs in massive stars. Section ?? describes the evolution of a massive star after the onset of hydrogen-burning in the core up until the final stage of evolution before the star ends its life. This leads onto Section ?? which reviews the eventual fate of massive stars.

1.1.1 Birth

Massive stars, as with lower mass stars, begin their lives within giant molecular clouds (GMCs), which are regions consisting of large clumps of interstellar material which have become over-dense with respect to the surrounding interstellar medium. These clouds are typically 10^4 – $10^7 M_\odot$, extend over 50–100pc and represent the densest parts of the interstellar medium (?). In a high-mass molecular cloud, high- and low-mass star formation takes place. Studies suggest that as the mass of the cloud decreases, so does the mass of the largest stars (??); however, recent studies suggest that this may not be a universal property (e.g. ?).

Within GMCs, over-dense regions continue to grow and eventually fragment into smaller cores. If these dense cores consist of a region where the local mass is greater than the associated Jeans mass for the region, the region is unstable to gravitational collapse. As the region collapses into a protostellar core, the optical depth increases, which gives rise to a large increase in temperature (?). The collapse proceeds until the radiation pressure exerted by the core is able to resist the gravitational collapse. The system is now in hydrostatic equilibrium and evolution proceeds through accretion. The collapsed core accretes matter from a surrounding disk which has condensed around the protostar. Meanwhile, the core of the protostar contracts and increases the temperature of the core towards hydrogen-burning temperatures. A larger protostar can accrete a larger amount of additional material from its surroundings and in turn grows to become a more massive star. In lower mass stars, accretion ceases before the star reaches the main sequence; however, a more massive star can perturb a larger amount of material and hence continues to accrete matter even after the hydrogen-burning phase has begun in its core. The ignition of hydrogen classically ends the period of formation, as the star now has a central energy source which governs the evolution

for the remainder of time spent on the main sequence. However, massive stars have one more crucial role to play in the process of star formation. Massive stars end their lives as supernovae, ejecting fusion products back into the environment from which they were born. The surrounding gas is shocked and compressed by this mass ejection event which can be the catalyst needed to produce more star formation in these environments (triggered star formation).

This is a very simplistic, qualitative overview of the formation of massive stars. In reality the exact processes governing these main stages of formation are complicated by various factors, for example, the effect of turbulence has been completely neglected in this discussion but has a vital role in many phases of star formation (?). The relative importance of each of the processes involved is not well understood. As of yet, there is no universal theory of how star formation proceeds in massive stars.

There are several crucial differences between low- and high-mass star formation.¹ Massive stars have larger temperatures and hence produce a large amount of ionising photons. This means that the accretion disk and outer envelope surrounding the massive star is photoevaporated and dissociated through interactions with these high energy photons. As alluded to previously, massive stars continue to accrete matter while on the hydrogen-burning main sequence (?). Whereas, lower mass stars ($<0.2M_{\odot}$) spend at least 10 Myrs evolving towards hydrogen fusion (?). A key difference in the star formation across a large mass range is the role of accretion. In lower mass star formation, accretion does not form significant amounts of the final mass of the star (?), whereas in higher mass star formation, accretion is generally accepted as a key role in accumulating the mass of the star (?).

Exactly how accretion acts is subject to much debate. Accretion is likely to proceed via competitive accretion (?). This is where a large fraction of the star is accreted from its surrounding material. In this scenario, the amount of material available for accretion is limited only by the surrounding environment. A star at the centre of the potential well of the surrounding gas cloud will be able to accrete more material than a star on the outskirts and hence will grow larger. As the star grows larger, it is able to accrete more and more matter. Eventually, neighbouring stars will be forced to compete for the surrounding gas, and in this

¹The opinion in the literature seems to suggest that low-mass star formation continues as normal up until around $\sim 20M_{\odot}$ (??), above this, star formation must take into account various complicating factors (see text).

Figure 1.1 *Hertzsprung–Russel diagram displaying evolutionary tracks of stars in the mass range $0.8 < M/M_{\odot} < 120$ taken from ?.*

scenario, the largest star (i.e. the star at the centre of the potential well) will be able to accrete a larger amount of material (for a useful economical analogy, see Section 4.2 of ?). In competitive accretion theory, the mass of the star is determined entirely by the environment in which it resides in and not by the initial conditions of the collapse.

Other theories of massive star formation in this context are that presented by ?, where accretion occurs onto the protostar via a disk which is produced as a result of the monolithic collapse of the gas cloud (into the protostar). In this scenario, the mass of the star is limited to the combined total of the protostar and the accretion disk (?). However, this theory has difficulty explaining the observed multiplicity and clustering of massive O stars (???).

An alternative path (which explains the formation of the most massive stars) is through stellar collisions. During the merging of star clusters, where stellar densities are highest, massive star formation can proceed through stellar collisions, resulting in very massive stars concentrated at the centre of clusters (?).

1.1.2 The Circle of Life

All stars spend a majority of their active life fusing hydrogen to helium in their cores on the hydrogen-burning main sequence (MS). On the MS, all stars remain in a stable state of hydrostatic equilibrium and hence their evolution in terms of luminosity and temperature is small (?). Once massive stars exhaust their core hydrogen fuel, various stages of nuclear burning succeed, including core helium- and carbon-burning. During this evolution, the surface temperature decreases and stars appear increasingly redder at later stages of their evolution (right hand side of Figure ??). As massive stars evolve off the main sequence, they may pass through a RSG stage of evolution. Therefore, understanding the physical processes which take place on the MS is important, as these stars may, or may not, be the direct progenitors of RSG stars.

During core hydrogen-burning, stars more massive than $1.1M_{\odot}$ fuse hydrogen

to helium through the carbon–nitrogen–oxygen (CNO) cycle. In this case, convection is induced owing to the large temperature gradient established as a result of the high temperature dependence of the rate of the CNO cycle (T^{14}). As a result of convective mixing, the core can be described as homogeneous during the hydrogen-burning phase (?). Convection is an important feature of this stage of evolution as it increases the MS lifetime by increasing the amount of material available for fusion.

Some of the main issues with the current theory of convection are characterising the size of the convective overshoot region and the effects of semi-convection on stellar evolution. Convective overshooting acts to increase the mixing of material beyond the convective boundary, within a stable region. As a convective cell is accelerated towards the boundary of the convective layer, its momentum carries the cell beyond this region into a region of convective stability. This has several consequences for the evolution of the hydrogen-burning phase, which are direct results of convective overshooting increasing the amount of fuel available for consumption within the convective core. How large an evolutionary effect convective overshooting produces is not well constrained.

Convective overshooting is characterised by the parameter α in units of the local pressure scale height (H_P) (?). Various authors have placed constraints upon α by using observational techniques including, for example, measuring the width of the main sequence (??). These studies (along with many others) find values of $\alpha = 0.1\text{--}0.6$ (a recent example is ?, finding $\alpha = 0.335$).

Semi-convection is also an issue for more massive stars. This is because, in massive stars, opacity is dominated by electron scattering (?). Semi-convection is named as such because of a discrepancy between two different criterion for convection. This situation arises outside a fully convective zone where a chemical gradient (∇_μ) is established. Semi-convection acts to smooth out the chemical gradient outside the fully convective regions.

As the star evolves and more hydrogen is consumed, the mass of the convective core decreases (?). Eventually, the star consists of a pure helium core surrounded by a hydrogen-burning shell. The maximum mass of the helium core, with respect to the total stellar mass is determined by the Schönberg–Chandrasekhar limit ($q_{SC} \geq \frac{M_c}{M_{tot}}$; usually derived as $q_{SC} \sim 0.1$), above which an inert helium core is unstable to gravitational collapse. In stars in the mass range $3 < M/M_\odot < 12$, the Schönberg–Chandrasekhar limit is usually reached at the end of the

hydrogen-burning phase (?). At this point, the helium core collapses, increasing the core temperature and density sufficiently that core helium-burning can occur, halting the collapse in the process. In more massive stars ($> 12M_{\odot}$), core helium-burning can smoothly proceed without the need for core collapse, as the central temperature in these stars is sufficiently high (10^8K).

During this phase of evolution hydrogen-burning proceeds within a shell outside the core. For stars which exceed the Schönberg–Chandrasekhar limit, during core contraction the outer hydrogen envelope will expand owing to the ‘mirror principle’ of shell fusion.² As the outer envelope expands, the effective temperature decreases. In Figure ??, the star moves to the right (towards redder colours) where massive stars evolve into the RSG phase and lower mass stars become red giant branch stars. This phase of evolution proceeds on a Kelvin–Helmholtz timescale, which for a $7M_{\odot}$ star is around 5×10^5 years (?), i.e. incredibly short on an evolutionary timescale. The short timescale on which this evolutionary phase proceeds accounts for the observed Hertzsprung gap. The evolution towards the red is halted as core helium-burning switches on.

In massive stars above $12M_{\odot}$, core helium-burning is thought to ignite when the star appears as a blue supergiant (BSG) (????). The redward migration of BSG stars is dictated by an intermediate convective zone (?) present in the atmosphere of the star, and is more gradual than the redward evolution of less massive stars. Stars more massive than around $40M_{\odot}$ never become RSGs (???) and hence, there is a peak luminosity of RSGs in any given population. As these massive stars evolve towards the red edge of the Hertzsprung–Russell (HR) diagram, their luminosities approach that of their Eddington luminosities; this induces large mass loss episodes. As a result, these stars halt their evolution towards the RSG phase and evolve towards the blue and consequently into Wolf–Rayet (WR) stars (??), see $60M_{\odot}$ track and above in Figure ??.

For a $10M_{\odot}$ star, core helium-burning proceeds for around 4Myrs (?). As suggested above, in specific cases, not all of the helium-burning phase is spent as a RSG. The length of time spent during the RSG phase depends upon how core helium-burning ignites. If a star begins its helium-burning lifetime as a BSG and subsequently evolves into the RSG phase, naturally, the length of time spent as a RSG will be shorter. In addition to this, stars with masses in the range of $25 < M/M_{\odot} < 40$ are thought to evolve back from the RSG phase to the BSG

²This principle is not well understood, but its effects appear to be a universal feature of shell fusion.

phase while still burning helium in their cores (?).

This evolution of massive stars between the BSG and RSG phase seeds the idea that stars in these stages of evolution will fall into two categories: (i) stars which begin helium-burning in the RSG or BSG phase, or (ii) stars which began helium-burning in a different evolutionary state and have since evolved into either the RSG or BSG regime. Distinguishing these objects observationally is challenging. ? use radial pulsations to distinguish between models of BSGs, which ‘roughly agree’ with observations of NGC 300 and in the Galaxy. However, an analogue to this has not been identified in RSGs.

Regardless of how extended the external envelopes in these stars are, core helium-burning proceeds in an identical manner. Helium burning in general proceeds through the triple alpha process, via the reaction, $3\alpha \rightarrow {}^{12}\text{C} + \gamma$. However, as the number density of ${}^{12}\text{C}$ increases, the reaction ${}^{12}\text{C}(\alpha + \gamma){}^{16}\text{O}$ is of increasing importance, although the exact rates at which these reactions proceed is not well constrained. This process of nuclear burning is highly temperature sensitive (even more so than the CNO cycle); therefore, a convective core is once again induced. In addition to this, massive red helium-burning stars also have large outer convective envelopes (?), which means the star appears near the Hayashi limit for a fully convective star in the HR diagram. The convective envelope dominates the evolution of all but the most massive RSGs ($30 < M/M_{\odot} < 40$) which do not appear as close to the Hayashi limit as their lower mass counterparts (see Figure 1 in ?).

At the end of the core helium-burning phase, a massive star contains a carbon/oxygen core surrounded by a helium-burning shell, which is in turn surrounded by a hydrogen-burning shell. At this point, the situation in the core now resembles that of the stage before core helium-burning. An inert carbon/oxygen core contracts and heats up which ignites the core fuel. Stars with initial masses greater than around $8M_{\odot}$ are able to fuse carbon in their cores in a stable fashion. In order for lower mass stars to do so, a degenerate carbon core is required. Whether or not stars are able to begin core carbon-burning in a stable manner is usually the physical basis for distinguishing between ‘intermediate’ and ‘high’ mass stars. During this process, carbon fuses to form an unstable form of ${}^{24}\text{Mg}$ which then decays through three channels: (i) ${}^{24}\text{Mg}^* \rightarrow {}^{23}\text{Mg} + n + \gamma$, (ii) ${}^{24}\text{Mg}^* \rightarrow {}^{20}\text{Ne} + \alpha + \gamma$, (iii) ${}^{24}\text{Mg}^* \rightarrow {}^{23}\text{Na} + p + \gamma$. Oxygen does not fuse at this stage of the evolution of the star and therefore the length of time a star spends fusing carbon depends strongly on the amount of carbon processing present in

the helium-burning phase (namely, the reaction $^{12}\text{C}(\alpha + \gamma) ^{16}\text{O}$).

Once the carbon fuel has been exhausted in the core, shell carbon-burning proceeds. The cycle of core contraction with new core reactants begins and subsequent neon-, oxygen- and silicon-burning in the core follow (?). As each new fuel in the core is exhausted, subsequent shell burning follows. Fusion reactions cease with ^{56}Fe as fusion reactions beyond this point are no longer energetically favourable.

Eventually, this leads to an ‘onion structure’ star, with an inert iron core surrounded by layers of lighter elements fusing in shells. These fusion reactions proceed on such a short timescale that the outer envelope does not have the time to react to the changing conditions in the core. This effectively ‘freezes out’ the outer envelope and the spectral type of the star does not change significantly during this period (?).

1.1.3 Death

Massive stars ($>8M_{\odot}$) end their lives as core-collapse supernovae (CCSN). These violent explosions are responsible for distributing elements synthesised within massive stars during their nuclear-burning lifetime, as well as during the explosion event. Observationally, CCSN are classed as type II, type Ib and type Ic.³ The classification of supernovae (SNe) is based on their optical spectra, specifically on the appearance of spectral features such as hydrogen and helium.

There are several different types of CCSN which occur as a result of the different conditions present in the cores of massive stars. For an in depth review see ?. For the purpose of this literature review, it will suffice to mention the four main CCSN channels: electron-capture SNe, iron-core SNe, gamma-ray burst SNe and pair-instability SNe. This review will focus on iron-core SNe in particular.

Iron-core SNe account for the majority of observed CCSN (???). This type of SNe are produced by massive stars which have initial masses above $\sim 9M_{\odot}$ (?). As mentioned in the previous section, massive stars conclude their nuclear-burning lifetimes with inert iron cores. Owing to a lack of energy generation, the core contracts and heats up. As the temperature reaches 10^{10}K , photons in the core of the star now have enough energy to photo-dissociate iron-group elements

³Type Ib and type Ic are often grouped as type Ibc, as the differences between these two types are difficult to distinguish (for example see ?).

Figure 1.2 *The evolutionary diversity of the end points of massive stars and their associated observed SN classification. Figure reproduced from ?. Acronym definitions: RSG, red supergiant; BSG, blue supergiant; LBV, luminous blue variable; WR, Wolf–Rayet; NS, neutron star; BH, black hole; GRB, gamma-ray burst; PISN, pair-instability supernova.*

into α particles. The increasing density forces electrons into nuclei and free protons, creating a neutron rich environment. As densities approach nuclear density, core contraction halts as a result of the repulsive force of the strong interaction (?). The in-falling outer layers crash into the core and the resulting shock-wave disrupts the entire star and produces the SN.

The exact mechanism which produces the SN explosion is subject to intense research, the subtleties of which will not be covered in this literature review. Recently, two extensive review articles (??) have been published on the subject giving a more in depth and complete overview of the subject.

In recent years, many SN progenitors have been discovered by reviewing extensive archival data available in the Local Group as well as through extensive dedicated SN surveys. These studies (or a quick review of the Central Bureau for Astronomical Telegrams (CBAT) list of SNe⁴) reveal that type II-P SNe are by far the most numerous type of CCSNe ($\sim 60\%$) and RSG stars are firmly established as their progenitors (?, and references therein). However, CCSN are observed in a variety of different types and hence, RSG stars are not the only type of massive star which can end their lives as SNe. Figure 1.2 illustrates the many possible channels towards SNe; this includes RSGs, BSGs, WRs and recently luminous blue variable (LBV) stars are being established as a part of this list (e.g. ??).

⁴<http://www.cbat.eps.harvard.edu/iau/cbat.html>

1.2 Chemical Properties of Red Supergiants

1.2.1 *J*-band Analysis Technique

1.2.2 Galactic and Extragalactic RSGs

The intrinsic brightness of RSGs, particularly in the NIR, makes these stars popular candidates for observations within and beyond the Galaxy. Studies of Galactic RSGs are used to derive fundamental stellar parameters such as radii, masses and distances. Galactic RSGs are also a natural starting point for extragalactic studies of larger populations of RSGs. Extragalactic observations have identified populations of RSG stars in a large range of galaxies within the Local Group and (in rarer cases) out to larger distances (e.g. ??????). These studies provide important results on RSGs in different environments. To illustrate this, this section first comments on some of the fundamental parameters derived using Galactic RSGs in Section 1.2.2 and summarises some of the important observational results regarding extragalactic RSGs in Section 1.2.2. In Sections 1.2.2 and ??, I focus on some of the aspects of extragalactic RSGs which will be applicable in later stages of this document.

Fundamental Parameters in Galactic RSGs

Research into Galactic RSGs is typically divided into two categories: studies of individual nearby stars such as Betelgeuse ($197 \pm 45\text{pc}$; ?) and VY CMa ($1420 \pm 120\text{pc}$; ?) and studies of populations of RSGs within open clusters and associations (e.g. ??). Studies of individual Galactic RSGs concentrate on the fundamental parameters of these stars such as their distances, mass-loss rates and circumstellar envelopes. Additionally, nearby Galactic RSGs are tests for detailed stellar atmosphere and evolutionary models.

Observations of Galactic RSGs reveal that they have large mass-loss rates ($10^{-(6 \pm 1)}\text{M}_{\odot}\text{yr}^{-1}$; ??) and extended circumstellar environments (?) which may contain masers (?). Mass loss during this phase of evolution is critical for the understanding of subsequent evolutionary stages as well as understanding SN progenitors. Galactic RSGs act as an important sample to study and understand the mechanisms of mass loss, as extragalactic observations are unable to resolve

the structure which can be seen in nearby Galactic stars.

One of the main uncertainties with studies of these nearby stars are the relatively poorly constrained distances (e.g., Betelgeuse with a distance uncertainty of nearly 25%). In order to (partially) remove the distance uncertainty problem, RSGs can be observed in Galactic clusters of known distances (e.g. ??). This technique is useful to study large populations of RSGs which can be used to test theories of star formation and models of RSGs and their atmospheres. Studies of RSGs in Galactic clusters are often used as a first test for studies which plan to include observations at larger distances (e.g. ???).

Extragalactic Studies and Results

Extragalactic studies of RSGs are advantaged in that it is possible to accumulate large samples of RSGs with which to test stellar evolution theories and derive stellar parameters. By using the different environments available in the Local Group, studies of extragalactic RSGs can probe a wide range of host galaxy parameter space. For example, M31 ($Z > 1.0Z_{\odot}$ in the central regions), a massive, metal-rich spiral galaxy and the Wolf–Lundmark–Melotte (WLM; $Z = 0.1Z_{\odot}$), a dwarf irregular, metal-poor galaxy, both contain a significant population of RSGs.

Through an analysis of RSGs in different metallicity environments, various authors report that the average spectral type of a RSG population is dependent upon metallicity (???), where lower metal abundances give rise to earlier average spectral types. In addition to this, RSGs can be used to measure abundances in Local Group galaxies, which yield important results by mapping metallicity gradients. This work has typically been done using high-resolution spectra at NIR wavelengths (???). However, in order to optimise these studies, ? adapted a method for determining the chemical properties of BSG stars in the optical (??), to RSGs in the NIR.

Measurements of the temperatures of RSGs have also provided insight through using observations of extragalactic RSGs in the NIR. The temperatures of RSG stars have been subject to debate for many years. There are many methods by which to estimate the effective temperature of a RSG star. The most popular of which is to fit the spectral energy distribution (SED) of the star with 1D model atmospheres (?). However, ? show that observations fitting models around the BVRI region, where molecular TiO lines dominate the absorption, result in a

systematically lower temperature compared with fitting the line-free continuum regions of the SED. This is due to the fact that the TiO molecular line forms higher in the atmosphere of the star than the continuum. This means that fitting the TiO region and assuming that the best fitting effective temperature is representative of the entire SED is not a good assumption. ? advocate using the entire SED *except* those regions dominated by the TiO absorption features. Deriving temperatures of extragalactic RSGs will be an important test for stellar evolution models and an excellent way in which to test models at different metallicities and in different environments.

In order to test models of stellar evolution against observations of extragalactic RSGs, a complete sample of RSG stars is clearly beneficial in order to draw conclusions on how the population behaves and evolves as a whole. In order to do this, generally, stars must be selected for spectroscopic follow-up observations based on their photometric properties.

Photometric Selection of RSGs

In the absence of spectroscopic observations, the selection of objects with respect to follow-up observations is often done using broad band photometry. This section will describe some of the various methods used to isolate a population of stars using magnitudes derived from broad band filters. This is important as good photometric selection of targets can optimise observing strategies and should be able to provide a complete sample of the population of stars.

Colour–magnitude diagrams (CMDs) are often used to isolate a particular type of star. A colour is defined as the difference between two magnitudes, derived from two different filters, and colours trace the temperature of a star (and hence their spectral type), whereas magnitude can be used to approximate luminosity. Therefore, using CMDs should allow the separation of a population of red, luminosity class I (supergiant), stars. However, using this method assumes that the sample consists purely of one population of stars at a given distance; if this assumption is not true, apparent magnitude is no longer sensitive to luminosity. For example, a nearby population of faint stars with similar spectral types (colours) could pose as a bright population of more distant objects. This becomes important when viewing an extended extragalactic object, such as a stellar cluster or external galaxy, at low Galactic latitude where the Galactic stellar density is highest. An example of a typical CMD is given in Figure ??.

=150mm bvcmd_all_eexample.eps

Figure 1.3 *Optical colour-magnitude diagram (CMD) of NGC 6822, in which the absolute V-band magnitude M_V , (corrected to the distance of NGC 6822) is plotted against $B-V$ colour. This figure illustrates how CMDs can be used to separate stars based on spectral type. Redder colours indicate later spectral types. This figure also demonstrates that CMDs have inherent degeneracies between different populations of stars: the central dense feature at $B-V \sim 1.0$ is attributed to foreground contaminants.*

=150mm bvrccd_eexample.eps

Figure 1.4 *Optical colour-colour diagram of NGC 6822. This figure illustrates the surface gravity dependence of the $B-V$ colour at a given $V-R$ colour. The population with the redder $B-V$ colours contain the RSG objects.*

To break the degeneracy between luminosity and distance, one can use colour-colour diagrams. Using multiple colour diagnostics can isolate stars based on more than just spectral type and absolute magnitude. ? show that at a given $V-R$ colour, the $B-V$ colour is sensitive to the surface gravity of a star. Therefore, given a $V-R$ colour, RSGs can be isolated owing to their low surface gravity. An example of such a colour-colour diagram is shown in Figure ?? where one can clearly see the distinction between low surface gravity RSG stars (with slightly redder $B-V$ colours) and the dwarf high surface gravity stars.

The selection of RSGs is typically done using a $B-V$, $V-R$ colour-colour diagram as this diagram has had much success in selecting RSGs and is known to contain a small number of contaminants. However, a potential issue with these diagrams as we move to extragalactic systems, which at the time of writing has not been quantified, is that RSGs are known to reside in dense regions and/or clusters with many bluer, younger stars. When viewing these stars in the optical, the colours from RSGs could potentially be contaminated to bluer colours by the blue stars which also reside nearby. In a $B-V$, $V-R$ diagram, this contamination would affect the completeness of the population of RSGs selected. As stated, this is not quantified and would require a comparison between the $B-V$, $V-R$ selection method with another known selection method and an analysis of the locations of the potentially contaminated RSG stars. A potential solution to this problem would be to select RSGs based on their NIR colours, which is where these stars are brightest and hence would be less subject to contamination to

nearby blue objects.

Working in the NIR, authors have used the J, J–K CMD (???) to select red stars (RSGs and asymptotic giant branch (AGB) stars) and much work has been done in identifying contaminants and the parameter space where individual populations reside in (?). As mentioned above, the main contaminants with this selection method are foreground dwarfs.

1.3 Chemical Evolution of Galaxies

The evolution of galaxies is a vast field and can be broadly split up into three main fields: dynamical, thermal and chemical evolution. The chemical evolution of galaxies governs the origin and distribution of elements within the host galaxy. This evolution principally depends upon galaxy and star formation. The initial origin and distribution of the chemical elements depends upon the galaxy formation process. Star formation acts to alter these quantities by creating, redistributing and removing chemical elements from the interstellar medium (ISM).

The lowest mass stars remove elements from the ISM by storing their gas and never evolving off the MS! Stars massive enough to evolve off the MS eject some mass during an AGB phase, but subsequently end their lives by removing elements from the ISM as passively cooling white dwarf stars. More massive stars undergo large amounts of mass loss during all phases of their evolution and end their lives by exploding as CCSNe, both of which act to alter the chemical composition of their surrounding gas clouds.

All three of these processes are important to take into account when studying how galaxies chemically evolve over time. However, quantifying contributions from these quantities is an involved process, complicated by a minefield of caveats and uncertainties.

Extragalactic observations of fundamental properties of galaxies play important roles in refining theories of galaxy formation and evolution. The mass–metallicity relationship (MZR; ?) of galaxies combines two fundamental parameters of galaxies. The stellar mass represents the amount of gas which star formation has removed from the ISM, whereas the present day galaxy metallicity represents how star formation has altered the initial ISM. Various authors have shown

that galaxy mass is proportional to metallicity (???). This relationship can be interpreted by considering multiple factors. In low-mass galaxies, outflows and SNe have a greater affect on the amount of material ejected from the host galaxy into the intracluster medium, owing to their shallower potential wells (e.g. ?). Additionally, low-mass galaxies represent an early stage in Galactic evolution and hence, these galaxies have not had time to process their gas into stars. As the host galaxy evolves, subsequent episodes of star formation increase the metal content of the galaxy (e.g. ?, and references therein).

MZR observations have typically relied upon ratios of strong oxygen emission lines (usually [OII], [OIII] relative to $H\beta$) from HII regions to derive metallicities of individual galaxies. This technique is used due to its applicability over a large distance range: ? use this technique in nearby galaxies whereas ? derive metallicity using this method in galaxies at $z > 3$. However, these measurements are known to be highly dependent upon the calibration method used (???). In order to provide an independent calibration of this method, BSG stars have been used to determine metallicity and abundance gradients in external galaxies (?). In addition to this, ? outline a method using RSGs as abundance probes with which to calibrate the MZR. These authors show that using a NIR window around $1.2\mu\text{m}$ (J-band) the dominant spectral features are that of strong metallic lines of iron and alpha elements (Ti, Mg, Si). These strong metallic lines allow abundance measurements from relatively low resolution spectra meaning that this technique can be used at distances of 3-4Mpc with an 8-10m class telescope (significantly, outside the Local Group).

Another advantage of using relatively low resolution spectra are that multi-object spectrographs can be used to observe extragalactic systems. This provides not only reliable abundances in nearby galaxies but also spatial information about abundances in these galaxies which allows the determination of metallicity gradients.

Therefore, extragalactic observations of RSG stars are important in order to provide independent constraints on some of the fundamental properties of Galactic formation and evolution. These studies have enormous potential in the era of extremely large telescope era which will be optimised for NIR observations.

Chapter 2

J-band Sythentic Spectral Fitting

Based on the work done by Davies et al. (2010) and Gazak (2014), I developed an implementation of the J-band synthetic spectral fitting software. This involves fitting the continuum between the observations and models and defining best fit model parameters for the stellar parameters, metallicity, effective temperature, surface gravity and microturbulence. The observations are fit with model spectra from a set of MARCS model atmospheres (Gustaffson et al. 2008).

2.0.1 Continuum Fitting

The continuum fitting procedure is important because there are many factors which can affect the level of the continuum. These factors include the resolution of the observations as well as the stellar parameters themselves. Intrinsically, when studying RSGs at medium resolution - owing to their cool atmospheres - there are many instances of blended spectral features. This density of spectral features creates a pseudo-continuum which in practice is never at the true continuum level. Figure 2.1 illustrates the varying continuum levels for models where the resolution is varied and Figure ?? shows this affect when varying only the metallicity.

Given that it is impossible to know the true continuum level from any given observation, any scaling applied must be consistent between the models and observations. Scaling is required not only to match the levels of the continuum placement, but also to match the line strengths between the models and observations. Providing the treatment of the models and observations are

Figure 2.1 *Models at different resolutions.*

consistent, the fact that the true continuum is never attained is not significant (Gazak et al., 2014b). For this procedure to work effectively, the observed and model spectra are required to have the same wavelength scale and spectral sampling. This is accounted for by degrading the sampling of the models to that of the observations by means of a linear interpolation. To ensure the spectra are on the same wavelength scale, the observed spectrum is cross-correlated with the model spectrum; a shift is then applied to the observed spectrum in order to minimise the cross-correlation matrix. Over this small wavelength range, one would not expect significant variations in the spectral resolution of the observations to perturb the cross-correlation.

To fit the continuum of the observations first I define the continuum width (cw) as:

$$cw = \frac{\lambda}{R} \times S, \quad (2.1)$$

where R is the resolution of the spectrum, λ is the wavelength at which the width is taken (in principle this wavelength varies across the spectrum, however, given our spectral window is sufficiently small, I assume $\lambda = 1.20\mu\text{m}$) and S is a scale factor which takes the range $0.5 < S < 1.0$. The continuum width is essentially the resolution element of the spectrum multiplied by the scale factor S . In Gazak et al. (2015 in press.) this scale factor is fixed at 0.5. The scale factor is introduced because ... ?

The model spectrum is divided into wavelength slices each of width $cw\mu\text{m}$ and the maximum of each slice is taken. Figure 2.2 illustrates that using this technique systematically removes absorption features from the spectrum. In this figure blue points represent the boundaries between the slices of width $cw\mu\text{m}$ and the maximum of each slice is shown in red. Any remaining features in this maximum spectrum are removed by rejecting outliers which are more than 3σ from the mean of the distribution. The remaining data points (P_{cont}) are then used to derive an initial correction function.

The aim of this process is to take the ratio the model to the data for all pseudo-continuum points. This ratio then defines the amount of scaling required for the model. The points at which to take this ratio are selected as described above. A

Figure 2.2 *Illustration of the continuum width (cw) and slicing the model spectrum into regions of $cw\mu m$ is able to remove structure in order to fit the continuum. The solid black line shows an example of a model spectrum degraded to a resolution of 3000, blue points show the boundaries between the slices and red points show the maximum of each slice. **Make this figure match Figure 2.1.***

third-order polynomial function is fit to this ratio (at P_{cont} only) to define the initial correction function (cf_1),

$$cf_1 = f\left(\frac{F_{mod}(P_{cont})}{F_{obs}(P_{cont})}\right) \quad (2.2)$$

where F_{mod} and F_{obs} are the flux in the model and observed spectrum respectively.

The final correction function (cf_2), a refinement of cf_1 , is defined by removing outliers more than 3σ from the mean of the correction function cf_1 .

Alternative methods of continuum fitting are discussed in Davies, Kudritzki & Figer (2010) and Evans et al. (2011). These methods select pseduo-continuum pixels in the models based on ranking the model pixels and selecting a percentage of the pixels with the largest flux. Providing the pixels from the model are selected in this manor and not those in the observations, this is a reliable method with which to derive the continuum level as demonstrated by Davies et al. (2015 in prep.). **What advantage (if any) does the method applied here have over the one used in Davies et al. (2015 in prep.)?**

2.0.2 Best Fit Parameters

Bibliography

- Asplund M., Grevesse N., Sauval A. J., Scott P., 2009, ARA&A, 47, 481
- Battinelli P., Demers S., Kunkel W. E., 2006, A&A, 451, 99
- Bergemann M., Kudritzki R.-P., Plez B., Davies B., Lind K., Gazak Z., 2012, ApJ, 751, 156
- Bergemann M., Kudritzki R.-P., Würl M., Plez B., Davies B., Gazak Z., 2013, ApJ, 764, 115
- Bovy J., Rix H.-W., 2013, ApJ, 779, 115
- Cioni M.-R. L. et al., 2014, A&A, 562, A32
- Davies B., Kudritzki R.-P., Figer D. F., 2010, MNRAS, 407, 1203
- Davies B. et al., 2013a, ApJ, 767, 3
- Davies R. I. et al., 2013b, A&A, 558, A56
- de Blok W. J. G., Walter F., 2000, ApJ, 537, L95
- de Blok W. J. G., Walter F., 2003, MNRAS, 341, L39
- de Blok W. J. G., Walter F., 2006, AJ, 131, 343
- Demers S., Battinelli P., Kunkel W. E., 2006, ApJ, 636, L85
- Doherty C. L., Siess L., Lattanzio J. C., Gil-Pons P., 2010, MNRAS, 401, 1453
- Efremova B. V. et al., 2011, ApJ, 730, 88
- Ekström S. et al., 2012, A&A, 537, A146
- Evans C. J. et al., 2011, A&A, 527, A50

- Gazak J. Z., Bastian N., Kudritzki R.-P., Adamo A., Davies B., Plez B., Urbaneja M. A., 2013, MNRAS, 430, L35
- Gazak J. Z. et al., 2014a, ApJ, 787, 142
- Gazak J. Z., Davies B., Kudritzki R., Bergemann M., Plez B., 2014b, ApJ, 788, 58
- Georgy C. et al., 2013, A&A, 558, A103
- Gratier P., Braine J., Rodriguez-Fernandez N. J., Israel F. P., Schuster K. F., Brouillet N., Gardan E., 2010, A&A, 512, A68
- Gustafsson B., Edvardsson B., Eriksson K., Jørgensen U. G., Nordlund Å., Plez B., 2008, A&A, 486, 951
- Hernández-Martínez L., Peña M., Carigi L., García-Rojas J., 2009, A&A, 505, 1027
- Herwig F., 2005, ARA&A, 43, 435
- Houk N., Smith-Moore M., 1988, Michigan Catalogue of Two-dimensional Spectral Types for the HD Stars. Volume 4, Declinations -26° to -12° .
- Humphreys R. M., 1979, ApJ, 231, 384
- Huxor A. P., Ferguson A. M. N., Veljanoski J., Mackey A. D., Tanvir N. R., 2013, MNRAS, 429, 1039
- Hwang N., Lee M. G., Lee J. C., Park W.-K., Park H. S., Kim S. C., Park J.-H., 2011, ApJ, 738, 58
- Hwang N., Park H. S., Lee M. G., Lim S., Hodge P. W., Kim S. C., Miller B., Weisz D., 2014, ApJ, 783, 49
- Kirby E. N., Cohen J. G., Guhathakurta P., Cheng L., Bullock J. S., Gallazzi A., 2013, ApJ, 779, 102
- Komiyama Y. et al., 2003, ApJ, 590, L17
- Koribalski B. S. et al., 2004, AJ, 128, 16
- Lapenna E., Origlia L., Mucciarelli A., Lanzoni B., Ferraro F. R., Dalessandro E., Valenti E., Cirasuolo M., 2015, ApJ, 798, 23

- Lee H., Skillman E. D., Venn K. A., 2006, *ApJ*, 642, 813
- Letarte B., Demers S., Battinelli P., Kunkel W. E., 2002, *AJ*, 123, 832
- Levesque E. M., Massey P., 2012, *AJ*, 144, 2
- Massey P., Olsen K. A. G., Hodge P. W., Jacoby G. H., McNeill R. T., Smith R. C., Strong S. B., 2007, *AJ*, 133, 2393
- McConnachie A. W., 2012, *AJ*, 144, 4
- Muschielok B. et al., 1999, *A&A*, 352, L40
- Nieva M.-F., Przybilla N., 2012, *A&A*, 539, A143
- Nikolaev S., Weinberg M. D., 2000, *ApJ*, 542, 804
- Pagel B. E. J., Edmunds M. G., Smith G., 1980, *MNRAS*, 193, 219
- Richer M. G., McCall M. L., 1995, *ApJ*, 445, 642
- Schaller G., Schaerer D., Meynet G., Maeder A., 1992, *A&AS*, 96, 269
- Schlegel D. J., Finkbeiner D. P., Davis M., 1998, *ApJ*, 500, 525
- Sharples R. et al., 2013, *The Messenger*, 151, 21
- Sibbons L. F., Ryan S. G., Cioni M.-R. L., Irwin M., Napiwotzki R., 2012, *A&A*, 540, A135
- Tolstoy E., Irwin M. J., Cole A. A., Pasquini L., Gilmozzi R., Gallagher J. S., 2001, *MNRAS*, 327, 918
- Venn K. A. et al., 2001, *ApJ*, 547, 765
- Weisz D. R., Dolphin A. E., Skillman E. D., Holtzman J., Gilbert K. M., Dalcanton J. J., Williams B. F., 2014, *ApJ*, 789, 147
- Wolfire M. G., McKee C. F., Hollenbach D., Tielens A. G. G. M., 2003, *ApJ*, 587, 278
- Woo J., Courteau S., Dekel A., 2008, *MNRAS*, 390, 1453
- Wood P. R., Bessell M. S., Fox M. W., 1983, *ApJ*, 272, 99

Chapter 3

Near-IR selection of Red Supergiants

A glorious paper on M33 where RSGs are selected based on their near-IR properties

30% complete?

Chapter 4

KMOS Observations in NGC 6822

4.1 Introduction

A promising new method to directly probe chemical abundances in external galaxies is with J -band spectroscopy of red supergiant (RSG) stars. With their peak flux at $\sim 1\,\mu\text{m}$ and luminosities in excess of $10^4 L_\odot$, RSGs are extremely bright in the near-IR, making them potentially useful tracers of the chemical abundances of star-forming galaxies out to large distances. To realise this goal, Davies, Kudritzki & Figer (2010) outlined a technique to derive metallicities of RSGs at moderate spectral resolving power ($R \sim 3000$). This technique has recently been refined using observations of RSGs in the Magellanic Clouds (?) and Perseus OB-1 (Gazak et al., 2014b). Using absorption lines in the J -band from iron, silicon and titanium, one can estimate metallicity ($[Z] = \log Z/Z_\odot$) as well as other stellar parameters (effective temperature, surface gravity and microturbulence) by fitting synthetic spectra to the observations. Owing to their intrinsic brightness, RSGs are ideal candidates for studies of extragalactic environments in the near-IR.

To make full use of the potential of RSGs for this science, multi-object spectrographs operating in the near-IR on 8-m class telescopes are essential. These instruments allow us to observe a large sample of RSGs in a given galaxy, at a wavelength where RSGs are brightest. In this context, the K -band Multi-Object Spectrograph (KMOS; Sharples et al., 2013) at the Very Large Telescope (VLT), Chile, is a powerful facility. KMOS will enable determination of stellar

abundances for RSGs out to distances of ~ 10 Mpc. Further ahead, a near-IR multi-object spectrograph on a 40-m class telescope, combined with the excellent image quality from adaptive optics, will enable abundance estimates for individual stars in galaxies out to tens of Mpc, a significant volume of the local universe containing entire galaxy clusters (Evans et al., 2011).

Here we present KMOS observations of RSGs in the dwarf irregular galaxy NGC 6822, at a distance of ~ 0.46 Mpc (McConnachie, 2012, and references therein). Chemical abundances have been determined for its old stellar population (e.g. Tolstoy et al., 2001; Kirby et al., 2013), but knowledge of its recent chemical evolution and present-day abundances is somewhat limited. Observations of two A-type supergiants by Venn et al. (2001) provided a first estimate of stellar abundances, finding $\log(\text{Fe}/\text{H})+12 = 7.01 \pm 0.22$ and $\log(\text{O}/\text{H})+12 = 8.36 \pm 0.19$, based on line-formation calculations for these elements assuming local thermodynamic equilibrium (LTE). A detailed non-LTE study for one of these objects confirmed the results finding 6.96 ± 0.09 for iron and 8.30 ± 0.02 for oxygen (?). Compared to solar values of 7.50 and 8.69, respectively (Asplund et al., 2009), this indicates abundances that are approximately one third solar in NGC 6822. A study of oxygen abundances in HII regions (Lee, Skillman & Venn, 2006) found a value of 8.11 ± 0.1 , confirming the low metallicity.

NGC 6822 is a relatively isolated Local Group galaxy, which does not seem to be associated with either M31 or the Milky Way. It appears to have a large extended stellar halo (Letarte et al., 2002; Hwang et al., 2014) as well as an extended HI disk containing tidal arms and a possible HI companion (de Blok & Walter, 2000). The HI disk is orientated perpendicular to the distribution of old halo stars and has an associated population of blue stars (de Blok & Walter, 2003; Komiyama et al., 2003). This led Demers, Battinelli & Kunkel (2006) to label the system as a ‘polar ring galaxy’. A population of remote star clusters aligned with the elongated old stellar halo have been discovered (Hwang et al., 2011; Huxor et al., 2013). In summary, the extended structures of NGC 6822 suggest some form of recent interaction.

In addition, there is evidence for a relatively constant star-formation history within the central 5 kpc (Weisz et al., 2014) with multiple stellar populations (Battinelli, Demers & Kunkel, 2006; Sibbons et al., 2012). This includes evidence for recent star formation in the form of a known population of massive stars, as well as a number of HII regions (Venn et al., 2001; de Blok & Walter, 2006; Hernández-Martínez et al., 2009; Levesque & Massey, 2012).

In this paper we present near-IR KMOS spectroscopy of RSGs in NGC 6822 to investigate their chemical abundances. In Section 4.2 we describe the observations. Section 4.3 describes the data reduction and Section 4.4 details the derived stellar parameters and investigates the spatial distribution of the estimated metallicities in NGC 6822. In Section 4.5 we discuss our results and Section 4.6 concludes the paper.

4.2 Observations

4.2.1 Target Selection

Our targets were selected from optical photometry (Massey et al., 2007), combined with near-IR (JHK_s) photometry (for details see Sibbons et al., 2012) from the Wide-Field Camera (WFCAM) on the United Kingdom Infra-Red Telescope (UKIRT). The two catalogues were cross-matched and only sources classified as stellar in the photometry for all filters were considered.

Our spectroscopic targets were selected principally based on their optical colours, as defined by ? and Levesque & Massey (2012). Figure 4.1 shows cross-matched stars, with the dividing line at $(B - V) = 1.25 \times (V - R) + 0.45$. All stars redder than this line, above a given magnitude threshold and with $V - R > 0.6$, are potential RSGs.

Distinguishing between RSGs and the most luminous stars on the asymptotic giant branch (AGB) is difficult owing to their similar temperatures and overlapping luminosities. Near-IR photometry can help to delineate these populations, with RSGs located in a relatively well-defined region in the near-IR ($J - K$) colour-magnitude diagram (CMD), as discussed by Nikolaev & Weinberg (2000). The near-IR CMD from the WFCAM data is shown in Figure 4.2 and was used to further inform our target selection. Employing the updated CMD criteria from Cioni et al. (2014) – modified for the distance and reddening to NGC 6822 – all of our potential targets from the combined optical and near-IR criteria are (notionally) RSGs.

The combined selection methods yielded 58 candidate RSGs, from which 18 stars were observed with KMOS, as shown in Figure 4.3. The selection of the final targets was defined by the KMOS arm allocation software KARMA (?), where the

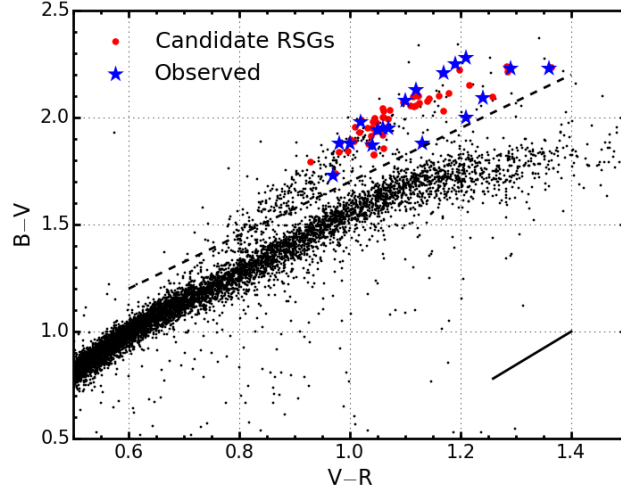


Figure 4.1 *Two-colour diagram for stars with good detections in the optical and near-IR photometry in NGC 6822. The black dashed line marks the selection criteria using optical colours, as defined by Levesque & Massey (2012). Red circles mark all stars which satisfied our selection criteria. Large blue stars denote targets observed with KMOS. The solid black line marks the foreground reddening vector for $E(B - V) = 0.22$ (Schlegel, Finkbeiner & Davis, 1998).*

field centre was selected to maximise the number of allocated arms, with priority given to the brightest targets. Optical spectroscopy of eight of our observed stars, confirming them as RSGs, was presented by Levesque & Massey (2012).

4.2.2 KMOS Observations

The observations were obtained as part of the KMOS Science Verification program on 30 June 2013 (PI: Evans, 60.A-9452(A)), with a total exposure time of 2400 s (comprising 8×300 s detector integrations). KMOS has 24 deployable integral-field units (IFUs) each of which covers an area of 28×28 within a 72 field-of-view. The 24 IFUs are split into three groups of eight, with the light from each group relayed to different spectrographs.

Offset sky frames (05 to the east) were interleaved between the science observations in an object (O), sky (S) sequence of: O, S, O, O. The observations were performed with the YJ grating (giving coverage from 1.02 to $1.36 \mu\text{m}$); estimates of the mean delivered resolving power for each spectrograph (obtained from the KMOS/esorex pipeline for two arc lines) are listed in Table 4.1.

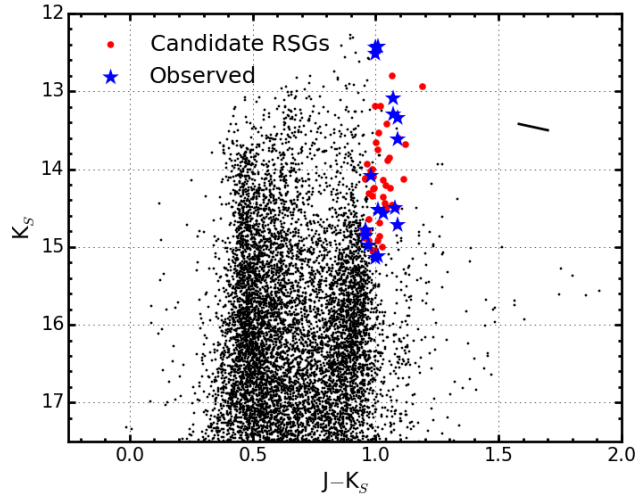


Figure 4.2 *Near-IR colour-magnitude diagram (CMD) for stars classified as stellar sources in the optical and near-IR catalogues, plotted using the same symbols as Figure 4.1. This CMD is used to supplement the optical selection. The solid black line marks the foreground reddening vector for $E(B - V) = 0.22$ (Schlegel, Finkbeiner & Davis, 1998).*

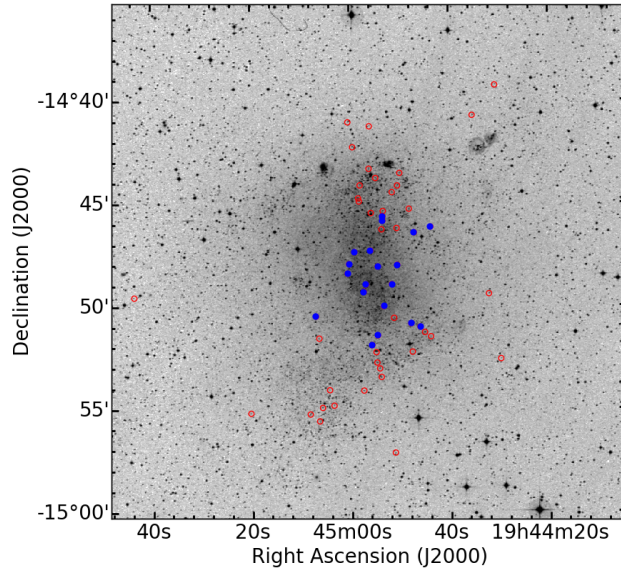


Figure 4.3 *Spatial extent of the KMOS targets over a Digital Sky Survey (DSS) image of NGC 6822. Blue filled circles indicate the locations of the observed red supergiant stars. Red open circles indicate the positions of red supergiant candidates selected using out photometric criteria (see Section 4.2.1).*

Table 4.1 *Measured velocity resolution and resolving power across each detector.*

Det.	IFUs	Ne $\lambda 1.17700 \mu\text{m}$		Ar $\lambda 1.21430 \mu\text{m}$	
		FWHM [km s^{-1}]	R	FWHM [km s^{-1}]	R
1	1-8	88.04 ± 2.67	$3\,408 \pm 103$	85.45 ± 2.67	$3\,511 \pm 110$
2	9-16	82.83 ± 2.48	$3\,622 \pm 108$	80.30 ± 3.05	$3\,736 \pm 142$
3	17-24	103.23 ± 2.73	$2\,906 \pm 77$	101.25 ± 2.99	$2\,963 \pm 87$

Table 4.2 *Summary of VLT-KMOS targets in NGC 6822.*

ID	S/N	α (J2000)	δ (J2000)	B	V	R	J	H	K_s	RV (km s^{-1})	Notes
NGC6822-RSG01	223	19:44:43.81	-14:46:10.7	20.83	18.59	17.23	14.16	13.37	13.09	-69.9 ± 3.7	Sample
NGC6822-RSG02	120	19:44:45.98	-14:51:02.4	20.91	18.96	17.89	15.53	14.72	14.52	-66.4 ± 6.6	Sample
NGC6822-RSG03	94	19:44:47.13	-14:46:27.1	21.30	19.41	18.41	16.13	15.35	15.12	-43.0 ± 6.0	
NGC6822-RSG04	211	19:44:47.81	-14:50:52.5	20.74	18.51	17.22	14.37	13.58	13.30	-64.5 ± 3.1	LM12
NGC6822-RSG05	104	19:44:50.54	-14:48:01.6	20.83	18.95	17.97	15.75	14.98	14.79	-93.4 ± 17.1	
NGC6822-RSG06	105	19:44:51.64	-14:48:58.0	21.33	19.45	18.32	15.81	14.95	14.72	...	
NGC6822-RSG07	145	19:44:53.46	-14:45:52.6	20.36	18.43	17.38	15.06	14.30	14.08	-72.6 ± 3.5	LM12
NGC6822-RSG08	103	19:44:53.46	-14:45:40.1	20.88	19.14	18.17	15.95	15.16	14.98	-73.0 ± 5.8	LM12
NGC6822-RSG09	201	19:44:54.46	-14:48:06.2	20.56	18.56	17.35	14.43	13.67	13.34	-79.9 ± 3.7	LM12
NGC6822-RSG10	302	19:44:54.54	-14:51:27.1	19.29	17.05	15.86	13.43	12.66	12.42	-57.2 ± 4.7	LM12
NGC6822-RSG11	327	19:44:55.70	-14:51:55.4	19.11	16.91	15.74	13.43	12.70	12.43	-67.9 ± 3.1	LM12
NGC6822-RSG12	100	19:44:55.93	-14:47:19.6	21.43	19.56	18.52	16.14	15.33	15.14	-61.2 ± 6.4	LM12
NGC6822-RSG13	106	19:44:56.86	-14:48:58.5	21.05	19.06	18.04	15.81	15.05	14.85	-55.0 ± 10.0	
NGC6822-RSG14	284	19:44:57.31	-14:49:20.2	19.69	17.41	16.20	13.52	12.76	12.52	-52.7 ± 4.4	LM12
NGC6822-RSG15	124	19:44:59.14	-14:47:23.9	21.30	19.17	18.05	15.58	14.74	14.50	-74.2 ± 13.4	
NGC6822-RSG16	107	19:45:00.24	-14:47:58.9	21.27	19.20	18.10	15.60	14.80	14.57	-68.8 ± 4.5	
NGC6822-RSG17	167	19:45:00.53	-14:48:26.5	20.84	18.75	17.51	14.70	13.86	13.61	-62.1 ± 4.0	Sample
NGC6822-RSG18	104	19:45:06.98	-14:50:31.1	21.06	19.12	18.06	15.74	14.94	14.78	-87.8 ± 9.4	Sample

Optical data from Massey et al. (2007), with typical photometric uncertainty 0.016, 0.006, 0.010 in B , V and R bands respectively. Near-IR data from the UKIRT survey (see Sibbons et al., 2012, for details), with typical errors 0.015, 0.010, 0.012, in J , H and K bands respectively. Targets observed by Levesque & Massey (2012) are indicated by ‘LM12’ in the final column (with their spectral classifications in parentheses). Targets used for abundance analysis are indicated by the comment ‘Sample’.

In addition to the science observations, a standard set of KMOS calibration frames were obtained consisting of dark, flat and arc-lamp calibrations (with flats and arcs taken at six different rotator angles). A telluric standard star was observed with the arms configured in the science positions, i.e. using the *KMOS_spec_cal_stdstarscipatt* template in which the standard star is observed sequentially through all IFUs. The observed standard was HIP97618, with a spectral type of B6 III (Houk & Smith-Moore, 1988).

A summary of the observed targets is given in Table 4.2. A signal-to-noise (S/N) ratio of 100 per resolution element is required for satisfactory results from this analysis method (see Gazak et al., 2014b). We estimated the S/N ratio of the spectra by comparing the counts in the brightest spatial pixels (within the 1.15-1.22 μm region) of each source with the counts in equivalent spatial pixels in the corresponding sky exposures (between the sky lines). The S/N estimated is knowingly an underestimate of the true S/N achieved.

4.3 Data Reduction

The observations were reduced using the recipes provided by the Software Package for Astronomical Reduction with KMOS (SPARK; Davies et al., 2013b). The standard KMOS/esorex routines were used to calibrate and reconstruct the science and standard-star data cubes as outlined by Davies et al. (2013b). Sky subtraction was performed using the standard KMOS recipes and telluric correction was performed using two different strategies. Throughout the following analysis all spectra have been extracted from their respective data cubes using a consistent method (i.e. the optimal extractions within the pipeline).

4.3.1 KMOS/esorex pipeline

The KMOS/esorex pipeline performs the initial calibrations by using a set of dark, flat and arc-lamp calibrations. These calibrations are all performed on raw KMOS images which contain 14x14 spectra from each IFU from the three spectrographs. The flat-field calibrations allow one to trace the spatial coordinates of each spectrum on the raw images. This information is then combined with the wavelength calibration information, obtained from the arc-lamp calibrations, to give a 14x14x2056 3-D spectrum for each IFU across the detector. A snapshot of the 14x14 spatial pixels is shown in Figure 4.4. When reducing multiple exposures of a single object, this cube is then combined with to produce the final data cube.

There are many routines with which to extract spectra from this final data cube. The simplest way to do this is to take the single brightest spectral pixel within the cube and extract a spectrum from that. However, higher signal-to-noise can be achieved by extracting the spectrum from a circular pixel mask centred on the brightest pixel, where each pixel is weighted by the integrated flux in that pixel.

4.3.2 Sky Subtraction

Sky subtraction is performed within the pipeline before IFU reconstruction where the science frame is matched with its nearest in time sky frame. Initial inspection of the extracted stellar spectra revealed minor residuals from the sky subtraction process. Reducing these cases with the ‘sky_tweak’ option within the KMOS/esorex reduction pipeline was ineffective to improve the subtraction of

these features. Any residual sky features could potentially influence our results by perturbing the continuum placement within the model fits, which is an important aspect of the fitting process (see Gazak et al., 2014b; ?, for more discussion). Thus, pending a more rigorous treatment of the data (e.g. to take into account the changing spectral resolution across the array), we exclude objects showing sky residuals from our analysis. Of the 18 observed targets, 11 were used to derive stellar parameters (as indicated in Table 4.2).

In-house Sky Subtraction

An alternative method of sky subtraction would be to subtract the sky from spatial pixels within the object IFU. This is possible as within each IFU the target does not extend over the entire set of spatial pixels as figure 4.4 demonstrates. Using a collection of these spatial pixels which contain little or no object flux can be a potential method for sky subtraction. Clearly this method has large potential benefits with respect to observing efficiency as less sky exposures would be needed for a given observing run. Theoretically, the sky subtraction from a region which is nearer in space to the object in question is beneficial in two different ways. The first is that the sky being subtracted more closely represents the sky background which the object is contaminated with. For comparison, during the sky exposures the telescope is offset by xx.xx arc-minutes, therefore, this sky exposure samples an intrinsically different atmospheric column when compared to the science exposure. Even though the differences in the sky lines on this spatial scale is small, as the signal originating from the sky is roughly an order of magnitude larger than that of our object, a small sky residual could affect the shape and/or strength of a genuine stellar feature. Secondly, the region of the host galaxy which the target object occupies will often contain contaminating flux. By sampling a region of space closer to the position of the target object, the underlying galaxy flux will be more accurately subtracted.

However, an inherent issue with this method of sky subtraction is that one may well remove some of the object flux in this process. Additionally, there is known to exist a slight difference in resolution over the spatial extent of the IFU (Lapenna et al., 2015) which could make comparisons between spatial pixels complicated. By standardising the resolution across the IFU one can potentially obtain a more reliable sky subtraction.

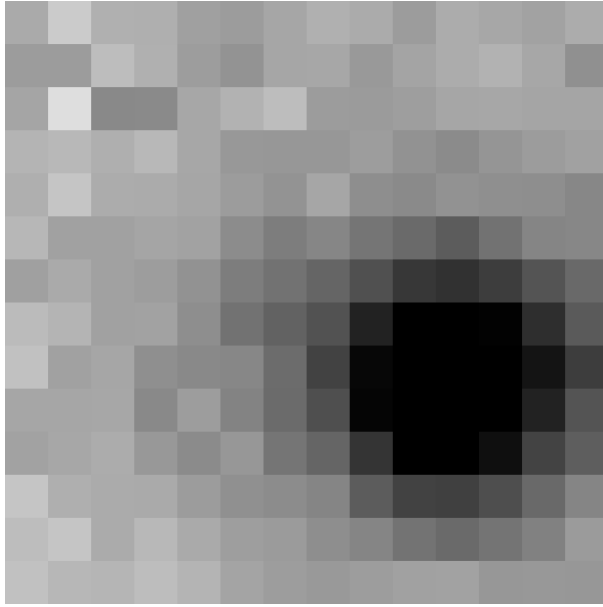


Figure 4.4 *Snapshot of a reconstructed KMOS IFU (at $\lambda = 1.16\mu\text{m}$) containing the science target NGC6822-RSG17. Darker shades indicate higher flux. This image serves to demonstrate that the target objects do not entirely fill the KMOS IFU. This therefore, presents the possibility for using several pixels which do not contain flux from the object in the sky subtraction process.*

4.3.3 Telluric Correction

One of the most important stages within the data reduction process, for our science, is the correction for the effects of the Earth’s atmosphere. As starlight passes through the atmosphere it is absorbed and re-emitted by various different molecules. These strong molecular features contaminate and blend genuine stellar features. In order to recover the stellar features a spectrum is derived which contains only the atmospheric absorption features. This spectrum is then used to correct the science spectrum.

Typically, one generates a telluric spectrum by observing an additional star of known spectral type. If the stellar features are well characterised for this spectral type, any additional features are assumed to be owing to the Earth’s atmosphere. The spectral type is usually chosen to minimize the number of stellar features present in the region of interest. In the J -band an A0V star has few lines of note and is therefore a good choice of telluric standard star in this regime. This method of telluric correction is robust and well tested and is the preferred method for many different studies. However, it does have some fairly fundamental limitations which include the fact that it is impossible to sample precisely the same atmospheric

column in both the science and telluric observations, as well as the additional time it takes to observe a standard star.

Recently, a tool for telluric correction which does not require standard star observations has been developed and tested on some VLT instruments (Smette et al. submitted). This package uses atmospheric modelling techniques to derive a telluric spectrum. The package is briefly explained in section 4.3.6, however, see Smette et al. (submitted) for a more thorough description.

4.3.4 Three-arm vs 24-arm Telluric Correction

The default template for telluric observations with KMOS is to observe a standard star in one IFU in each of the three spectrographs. However, there is an alternative template which allows users to observe a standard star in each of the 24 IFUs. This strategy should provide an optimum telluric correction for the KMOS IFUs but reduces observing efficiency.

A comparison between the two methods in the H -band was given by Davies et al. (2013b), who concluded that using the more efficient three-arm method was suitable for most science purposes. However, an equivalent analysis in the YJ -band was not available. To determine if the more rigorous telluric approach is required for our analysis, we observed a telluric standard star (HIP97618) in each of the 24 IFUs. This gave us the data to investigate both telluric correction methods and to directly compare the results.

We first compared the standard-star spectrum in each IFU with that used by the pipeline routines for the three-arm template in each of the spectrographs. Figure 4.5 shows the differences between the standard-star spectra across the IFUs, where the differences in the YJ -band are comparable to those in the H -band (cf. Fig.7 from Davies et al., 2013b). The qualitative agreement between the IFUs in our region of interest ($1.15\text{--}1.22\mu\text{m}$) is generally very good.

To quantify the difference the two telluric methods would make to our analysis, we performed the steps described in Section 4.3.5 for both templates. We then used the two sets of reduced science data (reduced with both methods of the telluric correction) to compute stellar parameters for our targets. The results of this comparison are detailed in Section 4.4.1.

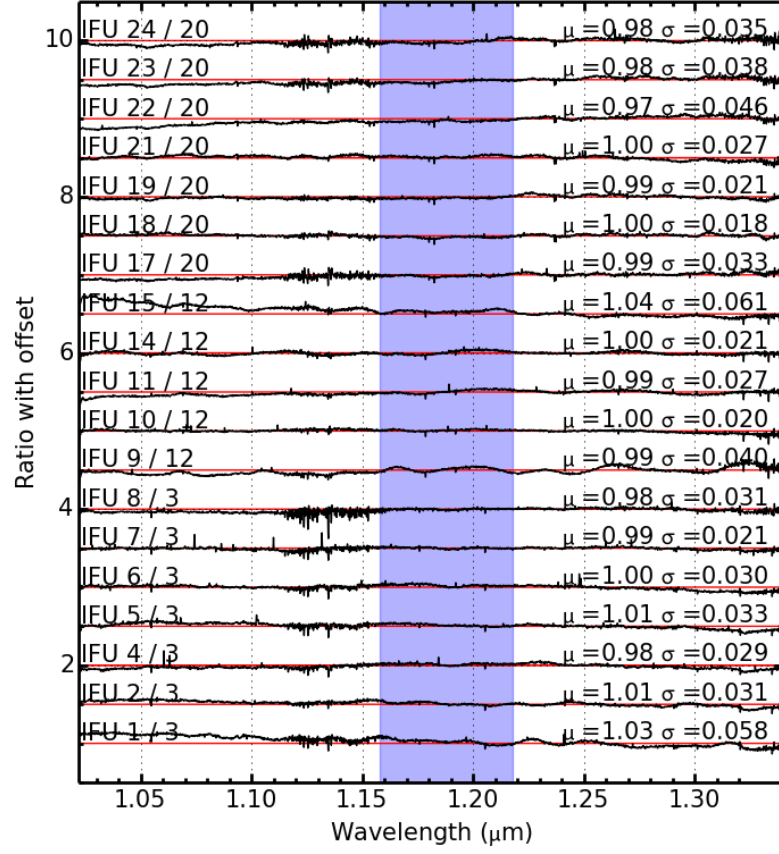


Figure 4.5 *Comparison of J-band spectra of the same standard star in each IFU. The ratio of each spectrum compared to that from the IFU used in the three-arm telluric method is shown, with their respective mean and standard deviation (μ and σ). Red lines indicate $\mu = 1.0$, $\sigma = 0.0$ for each ratio. The blue shaded area signifies the region used in our analysis, within which, the discrepancies between the IFUs are generally small. This is reflected in the standard deviation values when only considering this region. (IFUs 13 and 16 are omitted as no data were taken with these IFUs.)*

4.3.5 Telluric Correction Implementation

To improve the accuracy of the telluric correction, for both methods mentioned above, we implemented additional recipes beyond those of the KMOS/esorex pipeline. These recipes were employed to account for two effects which could potentially degrade the quality of the telluric correction. The first corrects for any potential shift in wavelength between each science spectrum and its associated telluric standard. The most effective way to implement this is to cross-correlate each pair of science and telluric-standard spectra. Any shift between the two is then applied to the telluric standard using a cubic-spline interpolation routine.

The second correction applied is a simple spectral scaling algorithm. This routine corrects for differences in line intensity of the most prominent features common to both the telluric and science spectra. To find the optimal scaling parameter the following formula is used,

$$T_2 = (T_1 + c)/(T_1 - c), \quad (4.1)$$

where T_2 is the corrected telluric-standard spectrum, T_1 is the initial telluric standard spectrum and c is the scaling parameter.

To determine the required scaling, telluric spectra are computed for $-0.5 < c < 0.5$, in increments of 0.02 (where a perfect value, i.e. no difference in line strength, would be $c = 0$). Each telluric spectrum is used to correct the science data and the standard deviation of the counts across the spectral region is computed for each corrected spectrum. The minimum value of the standard-deviation matrix defines the optimum scaling. For this algorithm, only the region of interest for our analysis is considered (i.e. $1.15\text{--}1.22\mu\text{m}$).

The final set of telluric-standard spectra from the KMOS/esorex reductions were modified using these additional routines and were then used to correct the science observations for the effects of the Earth's atmosphere.

4.3.6 MOLECFIT

As an alternative to observing telluric standard stars, a new telluric correction package, MOLECFIT, allows one to calculate a telluric spectrum based on

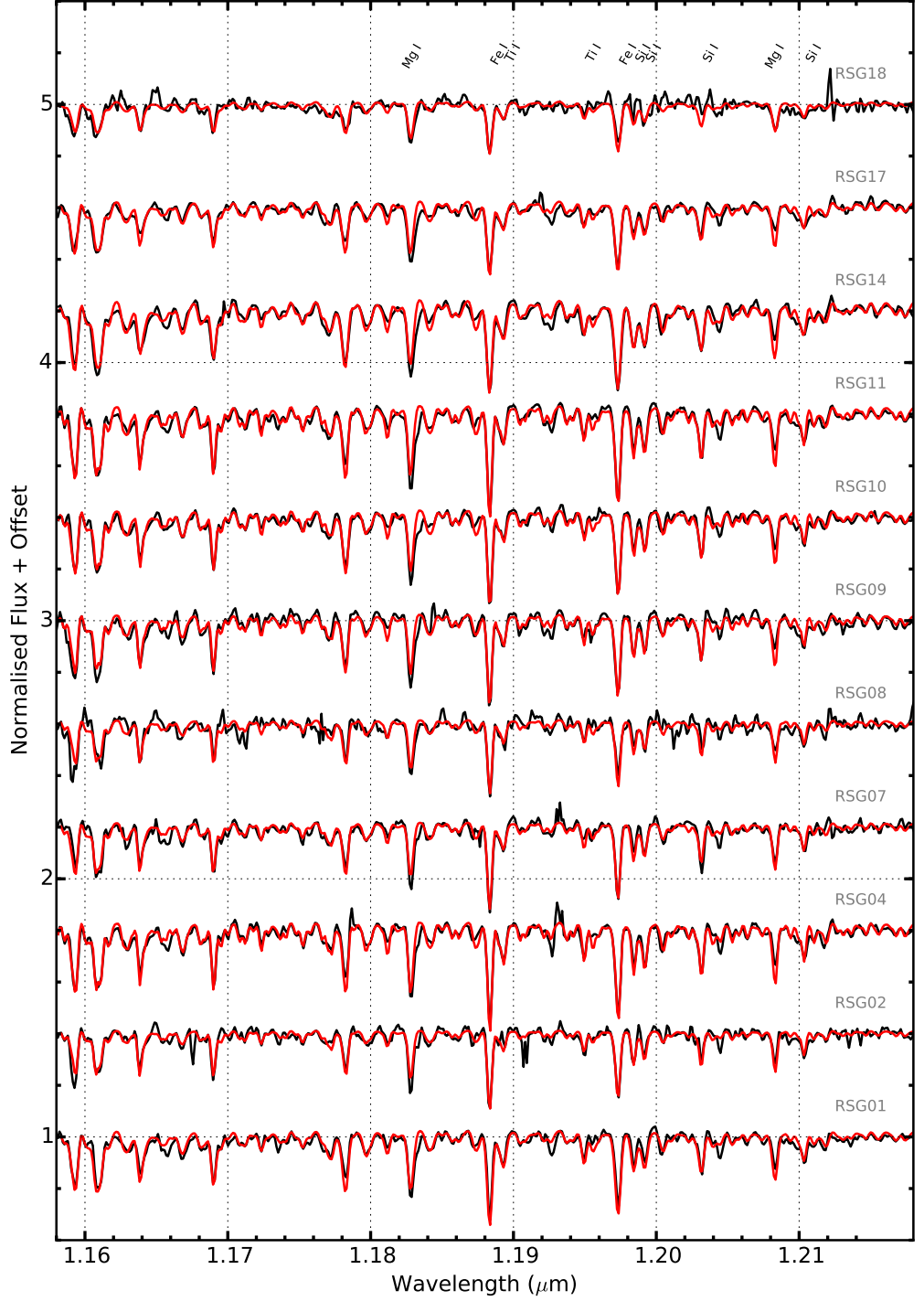


Figure 4.6 *KMOS spectra of the NGC 6822 RSGs and their associated best-fit model spectra (black and red lines, respectively). The lines used for the analysis from left-to-right by species are: $Fe\,I\lambda\lambda 1.188285, 1.197305, Si\,I\lambda\lambda 1.198419, 1.199157, 1.203451, 1.210353, Ti\,I\lambda\lambda 1.189289, 1.194954$. The two strong $Mg\,I$ lines are also labelled, but are not used in the fits (see Section 4.4).*

Table 4.3 *Cross-correlation shift values and rescaling (c) values.*

Name	24 AT		3 AT	
	Shift	c	Shift	c
NGC6822-RSG01	0.143	0.112	0.051	0.130
NGC6822-RSG02	0.135	0.140	0.184	0.216
NGC6822-RSG03	0.115	0.104	0.036	0.112
NGC6822-RSG04	0.133	0.122	0.133	0.122
NGC6822-RSG05	0.054	0.198	-0.017	0.206
NGC6822-RSG06	0.127	0.224	0.163	0.226
NGC6822-RSG07	-0.048	0.148	0.052	0.092
NGC6822-RSG08	0.062	0.180	0.062	0.180
NGC6822-RSG09	0.077	0.060	0.012	0.090
NGC6822-RSG10	-0.014	0.102	0.150	0.134
NGC6822-RSG11	0.067	0.134	0.060	0.110
NGC6822-RSG12	0.007	0.228	-0.019	0.182
NGC6822-RSG13	-0.329	0.290	-0.310	0.342
NGC6822-RSG14	-0.464	0.138	-0.021	0.258
NGC6822-RSG15	-0.324	0.206	-0.585	0.250
NGC6822-RSG16	-0.230	0.196	-0.207	0.244
NGC6822-RSG17	-0.192	0.160	-0.192	0.160
NGC6822-RSG18	-0.521	0.366	-0.458	0.364

atmospheric modelling. Briefly, the software uses a reference atmospheric profile to estimate the true profile for the time and location of the science observation. This model is then used to create a telluric spectrum which can be used to correct the observations.

This software has been shown to work well, on a variety of VLT instruments (Smette et al. submitted) and has been rigorously tested using X-shooter spectra (Kausch et al. submitted). However, the package has yet to be tested thoroughly on lower-resolution observations such as those from KMOS. Our first tests appear encouraging, however, pending further characterisation of the KMOS data cubes (e.g., small variations in spectral resolving power leading to sky residuals, see Section 4.3.2), we will investigate the potential of the MOLECFIT package in future papers of this series.

4.3.7 Stellar Radial Velocities

Radial velocities for each target are listed in Table 4.2. To check the accuracy of in the wavelength solution provided by the data reduction pipeline, this solution is cross-correlated with the wavelength solution of a spectrum of the Earth’s telluric features¹. In general, this is a small correction. The science spectra are then telluric corrected in the manner described above.

Radial velocities are estimated by measuring the peak of the cross-correlation function between the telluric-corrected science spectra (taking the spectrum from the brightest spatial pixel) and an appropriate synthetic RSG spectrum. The errors are calculated by taking the dispersion of each line used to derive the radial velocities scaled by the number of lines used, following Lapenna et al. (2015). A robust radial velocity could not be derived for one of our candidates (NGC6822-RSG06) owing to strong residual sky subtraction features, therefore, it is not considered further.

Radial velocities estimates are shown as a function of distance to the centre of NGC6822 in Figure 4.7. The average radial velocity for our targets is $-68 \pm 12 \text{ km s}^{-1}$, in good agreement with the systemic radial velocity of the HI disk ($-57 \pm 2 \text{ km s}^{-1}$; Koribalski et al., 2004). Our radial velocities also agree with estimates for the two A-type supergiants from Venn et al. (2001). This result

¹Retrieved from http://www.eso.org/sci/facilities/paranal/decommissioned/isaac/tools/spectroscopic_standards.html.

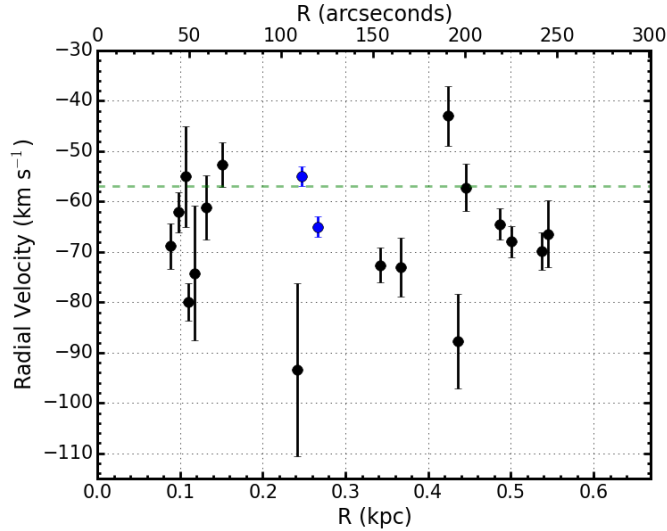


Figure 4.7 *Radial velocities of targets shown against their distance from the galaxy centre. The average radial velocity for the sample is $-68 \pm 12 \text{ km s}^{-1}$. The green dashed line indicates HI systemic velocity ($-57 \pm 2 \text{ km s}^{-1}$; Koribalski et al., 2004). The radial velocities of two A-type supergiants from Venn et al. (2001) are shown in blue.*

confirms that our candidates are NGC 6822 members.

4.4 Results

Stellar parameters (metallicity, effective temperature, surface gravity and micro-turbulence) have been derived using the *J*-band analysis technique described by Davies, Kudritzki & Figer (2010) and demonstrated by Gazak et al. (2014b) and ?. To estimate physical parameters this technique uses a grid of synthetic spectra to fit observational data, in which the models are degraded to the resolution of the observed spectra (Table 4.1). Model atmospheres were generated using the MARCS code (Gustafsson et al., 2008) where the range of parameters are defined in Table 4.4. The precision of the models is increased by including departures from LTE in some of the strongest Fe, Ti and Si atomic lines (Bergemann et al., 2012, 2013). The two strong magnesium lines in our diagnostic spectral region are excluded from the analysis at present as these lines are known to be affected strongly by non-LTE effects (see Figure 4.6, where the two Mg I lines are systematically under- and over-estimated, respectively). The non-LTE effects on the formation of the Mg I lines will be explored by Bergemann et al. (in prep).

Table 4.4 *Model grid used for analysis.*

Model Parameter	Min.	Max.	Step size
T_{eff} (K)	3400	4000	100
	4000	4400	200
$[Z]$ (dex)	-1.50	1.00	0.25
$\log g$ (cgs)	-1.0	1.0	0.5
ξ (km s ⁻¹)	1.0	6.0	1.0

Table 4.5 *Fit parameters for reductions using the two different telluric methods.*

Target	IFU	24 Arm Telluric				3 Arm Telluric		
		T_{eff} (K)	$\log g$	ξ (km s ⁻¹)	$[Z]$	T_{eff} (K)	$\log g$	ξ (km s ⁻¹)
NGC6822-RSG01	6	3790 ± 80	-0.0 ± 0.3	3.5 ± 0.4	-0.55 ± 0.18	3860 ± 90	-0.1 ± 0.5	3.5 ± 0.4
NGC6822-RSG02	11	3850 ± 100	0.4 ± 0.5	3.5 ± 0.4	-0.78 ± 0.22	3810 ± 110	0.4 ± 0.5	3.3 ± 0.4
NGC6822-RSG04	12	3880 ± 70	0.0 ± 0.3	4.0 ± 0.4	-0.32 ± 0.16	3880 ± 70	0.0 ± 0.3	4.0 ± 0.4
NGC6822-RSG07	2	3970 ± 60	0.4 ± 0.5	3.9 ± 0.4	-0.58 ± 0.19	3990 ± 80	0.1 ± 0.5	3.8 ± 0.4
NGC6822-RSG08	3	3910 ± 100	0.6 ± 0.5	3.0 ± 0.4	-0.58 ± 0.24	3910 ± 100	0.6 ± 0.5	3.0 ± 0.4
NGC6822-RSG09	4	3980 ± 60	0.1 ± 0.4	3.7 ± 0.4	-0.38 ± 0.16	3990 ± 80	-0.1 ± 0.5	3.6 ± 0.4
NGC6822-RSG10	14	3900 ± 80	-0.3 ± 0.5	3.7 ± 0.4	-0.67 ± 0.16	3850 ± 80	-0.3 ± 0.5	3.5 ± 0.4
NGC6822-RSG11	15	3870 ± 80	-0.4 ± 0.5	4.2 ± 0.5	-0.53 ± 0.19	3850 ± 60	-0.3 ± 0.4	4.3 ± 0.5
NGC6822-RSG14	17	3910 ± 110	-0.5 ± 0.5	3.6 ± 0.5	-0.20 ± 0.21	3880 ± 110	-0.5 ± 0.5	3.6 ± 0.4
NGC6822-RSG17	21	3890 ± 120	0.1 ± 0.5	3.0 ± 0.4	-0.43 ± 0.28	3890 ± 120	0.1 ± 0.5	3.0 ± 0.4
NGC6822-RSG18	18	3810 ± 130	0.4 ± 0.5	2.2 ± 0.4	-0.68 ± 0.31	3740 ± 130	0.4 ± 0.5	2.1 ± 0.4

4.4.1 Telluric Comparison

We used these Science Verification data to determine which of the two telluric standard methods is most appropriate for our analysis. Table 4.5 details the stellar parameters derived for each target using both telluric methods and these parameters are compared in Figure 4.8. The mean difference in metallicity from the two methods is $\Delta[Z] = 0.04 \pm 0.07$. Therefore, for our analysis, there is no significant difference between the two telluric approaches.

4.4.2 Stellar Parameters and Metallicity

Table 4.5 summarises the derived stellar parameters. For the remainder of this paper, when discussing stellar parameters, we adopt those derived using the 24-arm telluric method (i.e. the results in the left-hand part of Table 4.5.) The average metallicity for our sample of 11 RSGs in NGC 6822 is $\bar{Z} = -0.52 \pm 0.21$. This result is in good agreement with the average metallicity derived in NGC 6822 from blue supergiant stars (BSGs; Muschielok et al., 1999; Venn et al., 2001).

A direct comparison with metallicities from BSGs is legitimate as the results

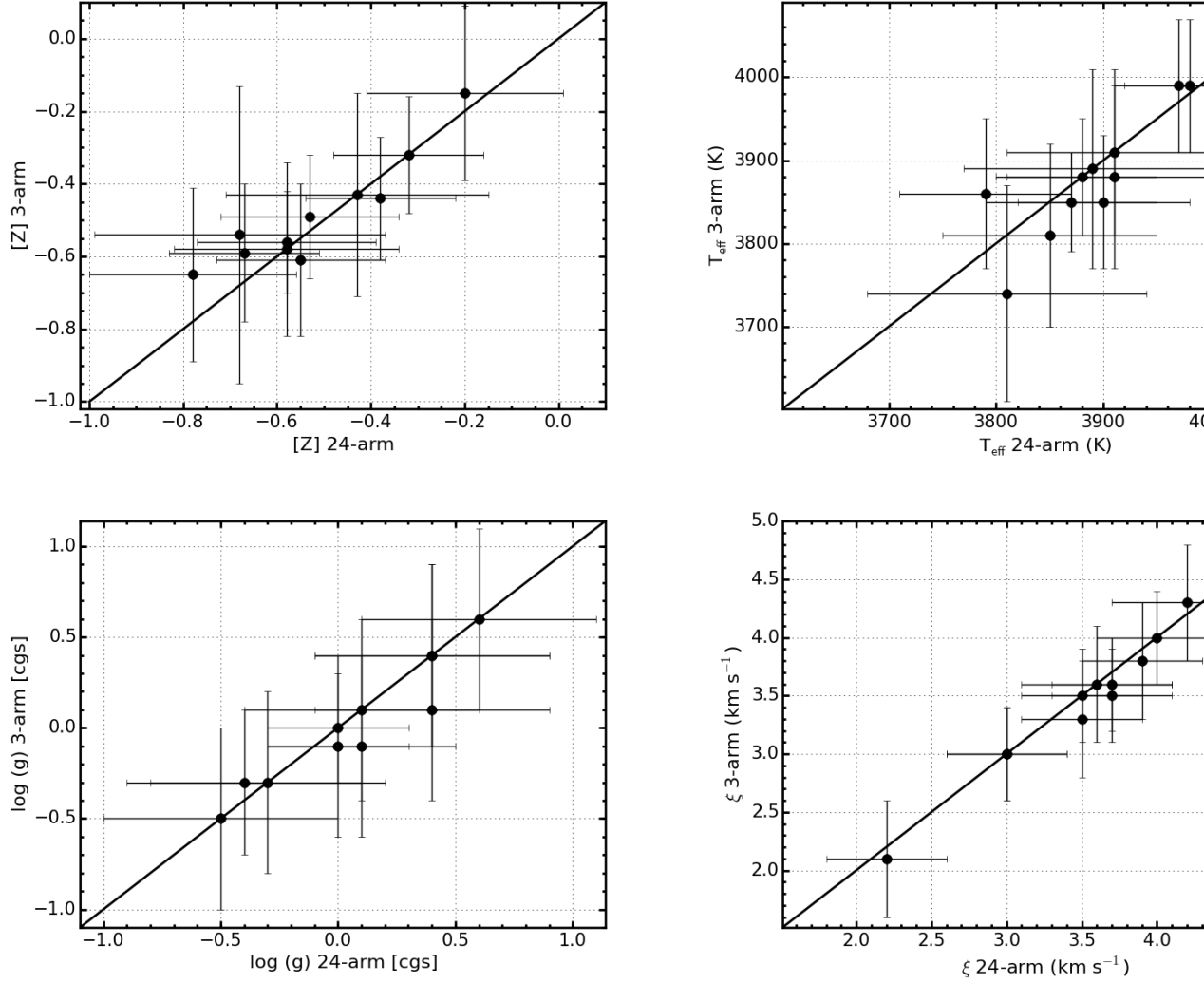


Figure 4.8 Comparison of the model parameters using the two different telluric methods. In each panel, the x-axis represents stellar parameters derived using the 3-arm telluric method and the y-axis represents those derived using the 24-arm telluric method. Top left: metallicity ($[Z]$), mean difference $\langle \Delta[Z] \rangle = 0.04 \pm 0.07$. Top right: effective temperature (T_{eff}), mean difference $\langle \Delta T_{\text{eff}} \rangle = -14 \pm 42$. Bottom left: surface gravity ($\log g$), mean difference $\langle \Delta \log g \rangle = -0.06 \pm 0.12$. Bottom right: Microturbulence (ξ), mean difference $\langle \Delta \xi \rangle = -0.1 \pm 0.1$. In all cases, the distributions are statistically consistent with a one-to-one ratio (black lines).

derived here yield a global metallicity ($[Z]$) which closely resembles the Fe/H ratio derived in Venn et al. (2001). While our $[Z]$ measurements are also affected by Si and Ti, we assume $[Z] = [\text{Fe}/\text{H}]$ for the purposes of our discussion. Likewise, we can compare oxygen abundances (relative to solar) obtained from HII regions as a proxy for $[Z]$ by introducing the solar oxygen abundance $12+\log(\text{O}/\text{H})_{\odot} = 8.69$ (Asplund et al., 2009) through the relation $[Z] = 12+\log(\text{O}/\text{H})-8.69$.

The RSG and BSG stages are different evolutionary phases within the life cycle of a massive star, while HII regions are the birth clouds which give rise to the youngest stellar population. As the lifetimes of RSGs and BSGs are $< 50\text{Myr}$, their metallicity estimates are also expected to be representative of their birth clouds.

To investigate the spatial distribution of chemical abundances in NGC 6822, in Figure 4.9 we show the metallicities of our RSGs as a function of radial distance from the centre of the galaxy, as well as the results from Venn et al. (2001) and the indicative estimates from Muschiolok et al. (1999).

A least-squares fit to the KMOS results reveals a low-significance abundance gradient within the central 1 kpc of NGC 6822 of $-0.5 \pm 0.4 \text{ dex kpc}^{-1}$. The extrapolated central metallicity from the fit (i.e. at $R=0$) of $[Z] = -0.30 \pm 0.15$ derived remains consistent with the average metallicity assuming no gradient.

Figure 4.10 shows the location of our sample in the Hertzsprung-Russell (H-R) diagram. Bolometric corrections were computed using the calibration in Davies et al. (2013a) to calculate luminosities. This figure shows that the temperatures derived using the J -band method are systematically cooler than the end of the evolutionary models (which terminate at the end of the carbon-burning phase for massive stars) for $Z = 0.002$ from Georgy et al. (2013). This is discussed in Section 4.5.2.

4.5 Discussion

4.5.1 Metallicity Measurements

We find an average metallicity for our sample of $\bar{Z} = -0.52 \pm 0.21$ which agrees well with the results derived from BSGs (Muschiolok et al., 1999; Venn et al.,

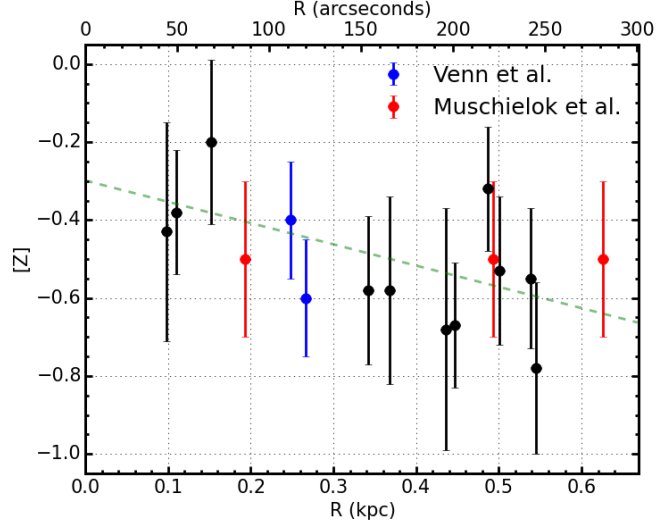


Figure 4.9 *Derived metallicities for 11 RSGs in NGC 6822 shown against their distance from the galaxy centre; the average metallicity is $\bar{Z} = -0.52 \pm 0.21$. Blue and red points show blue supergiants results from Venn et al. (2001) and Muschelok et al. (1999) respectively. A least-squares fit to the KMOS results reveals a low-significance abundance gradient (see text for details). For comparison, $R_{25} = 460$ ($= 1.03$ kpc; McConnachie, 2012).*

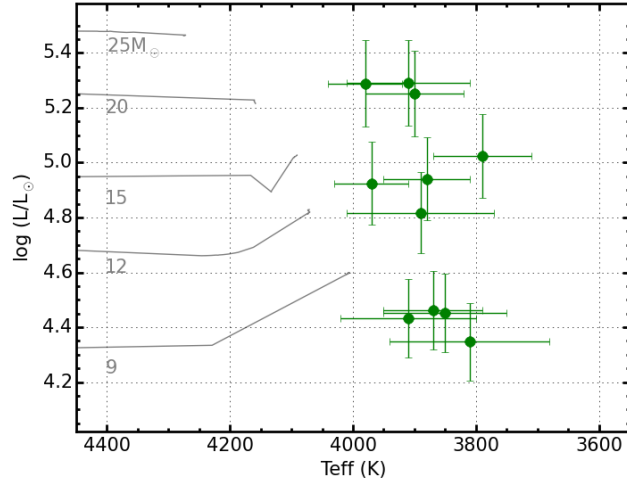


Figure 4.10 *H-R diagram for the 11 RSGs in NGC 6822. Evolutionary tracks including rotation ($v/v_c = 0.4$) for SMC-like metallicity ($Z = 0.002$) are shown in grey, along with their zero-age mass (Georgy et al., 2013). Bolometric corrections are computed using the calibration in Davies et al. (2013a). We note that compared to the evolutionary tracks, the observed temperatures of NGC 6822 RSGs are systematically cooler. This is discussed in Section 4.5.2.*

2001; ?) and HII regions (Lee, Skillman & Venn, 2006).

We also find evidence for a low-significance metallicity gradient within the central 1 kpc of NGC 6822 ($-0.5 \pm 0.4 \text{ dex kpc}^{-1}$ with a $\chi^2_{red} = 1.16$; see Figure 4.9). The gradient derived is consistent with the trend reported in Venn et al. (2001) from their results for the two BSGs compared with HII regions from Pagel, Edmunds & Smith (1980) and two planetary nebulae from Richer & McCall (1995) at larger galactocentric distances. Our result is also consistent with the gradient derived from a sample of 49 local star-forming galaxies (Ho et al. submitted). Including the results for BSGs from Venn et al. (2001) in our analysis, gives a consistent gradient ($-0.48 \pm 0.33 \text{ dex kpc}^{-1}$) with a smaller $\chi^2_{red} = 1.06$. Results from Muschielok et al. (1999) are not included in the fit as these measurements were qualitative estimates of metallicity.

In contrast, Lee, Skillman & Venn (2006) used the oxygen abundances from 19 HII regions and found no clear evidence for a metallicity gradient. Using a subset of the highest quality HII region data available, these authors found a gradient of $-0.16 \pm 0.05 \text{ dex kpc}^{-1}$. Including these results into our analysis degrades the fit and changes the derived gradient significantly ($-0.18 \pm 0.05 \text{ dex kpc}^{-1}$; $\chi^2_{red} = 1.78$). At this point it is not clear whether the indication of a gradient obtained from the RSGs and BSGs is an artefact of the small sample size, or indicates a difference with respect to the HII region study.

There have been a number of studies of the metallicity of the older stellar population in NGC 6822. From spectroscopy of red giant branch (RGB) stars, Tolstoy et al. (2001) found a mean metallicity of $[\text{Fe}/\text{H}] = -0.9$ with a reasonably large spread (see their Figure 19). More recently, Sibbons et al. (2012) derived metallicities using a population of AGB stars within the central 4 kpc of NGC 6822. They found an average metallicity of $[\text{Fe}/\text{H}] = -1.29 \pm 0.07 \text{ dex}$. Likewise, Kirby et al. (2013) used spectra of red giant stars within the central 2 kpc and found an average metallicity of $[\text{Fe}/\text{H}] = -1.05 \pm 0.49$. We note that none of these studies found any compelling evidence for spatial variations in the stellar metallicities, which is not surprising given that, in disc galaxies, radial migration is thought to smooth out any abundance gradients over time. The stellar populations used for these studies are known to be significantly older than our sample, therefore, owing to the chemical evolution in the time since the birth of the older populations, we expect the measured metallicities to be significantly lower.

The low metallicity of the young stellar population and the interstellar medium (ISM) in NGC 6822 can be understood as a consequence of the fact that it is a relatively gas-rich galaxy with a mass $M_{HI} = 1.45 \times 10^8 M_{\odot}$ (Koribalski et al., 2004) and a total stellar mass of ranging from $M_* = 0.83 - 1.70 \times 10^8 M_{\odot}$ (Weisz et al., 2014; Kirby et al., 2013; Woo, Courteau & Dekel, 2008).

The simple closed-box chemical-evolution model relates the metallicity mass fraction $Z(t)$ at any time to the ratio of stellar to gas mass $\frac{M_*}{M_g}$ through

$$Z(t) = \frac{y}{1-R} \ln \left[1 + \frac{M_*(t)}{M_g(t)} \right], \quad (4.2)$$

where y is the fraction of metals per stellar mass produced through stellar nucleosynthesis (the so-called yield) and R is the fraction of stellar mass returned to the ISM through stellar mass-loss.

According to Kudritzki et al. (in prep), the ratio $y/(1-R)$ can be empirically determined from the fact that the metallicity of the young stellar population in the solar neighbourhood is solar, with a mass fraction $Z_{\odot} = 0.014$ (Nieva & Przybilla, 2012). With a stellar-to-gas mass column density of 4.48 in the solar neighbourhood (Wolfire et al., 2003; Bovy & Rix, 2013) one then obtains $y/(1-R) = 0.0082 = 0.59 Z_{\odot}$ with an uncertainty of 15 percent dominated by the 0.05 dex uncertainty of the metallicity determination of the young population.

Accounting for the presence of helium and metals in the neutral interstellar gas we can turn the observed HI mass in NGC 6822 into a gas mass via $M_g = 1.36 M_{HI}$ and use the simple closed-box model to predict a metallicity of $[Z] = -0.44$ - -0.69 , in good agreement with our value obtained from RSG spectroscopy.

As discussed above, the older stellar population of AGB stars has a metallicity roughly 0.8 dex lower than the RSGs. In the framework of the simple closed-box model this would correspond to a period in time where the ratio of stellar to gas mass was ~ 0.1 (much lower than the present value of 0.42-0.86). The present star-formation rate of NGC 6822 is $\sim 0.02 M_{\odot} \text{yr}^{-1}$ (Gratier et al., 2010; Efremova et al., 2011). At such a high level of star formation it would have taken five Gyr to produce the presently observed stellar mass and to arrive from the average metallicity of the AGB stars to that of the young stellar population (of course, again relying on the simple closed-box model). Evidence suggests that the star-formation rate was substantially lower in the past (Weisz et al., 2014; Efremova

et al., 2011), therefore, the build up of the observed stellar mass would have taken correspondingly longer.

Given the irregularities present in the stellar and gaseous morphology of NGC 6822, this galaxy may not be a good example of a closed-box system, however it is remarkable that the closed-box model reproduces the observed metallicity so closely.

4.5.2 Temperatures of RSGs

Effective temperatures have been derived for 11 RSGs from our observed sample in NGC 6822. To date, this represents the fourth data set used to derive stellar parameters in this way and the first with KMOS. The previous three data sets which have been analysed are those of 11 RSGs in PerOB1, a Galactic star cluster (Gazak et al., 2014b), nine RSGs in the LMC and 10 RSGs in the SMC (both from ?). These results range from $Z=Z_{\odot}$ in PerOB1 to $Z=0.3Z_{\odot}$ in the SMC, around 0.5 dex in metallicity.

We compare the effective temperatures derived in this study to those of the previous results in different environments. Their distribution is shown as a function of metallicity in Figure 4.11. Additionally, Figure 4.12 shows the H-R diagram for the four sets of results. Bolometric corrections to calculate the luminosities for each sample were computed using the calibration in Davies et al. (2013a).

From these figures, we see no evidence for significant variations in the average temperatures of RSGs with respect to metallicity. This is in contrast to current evolutionary models which display a change of $\sim 450\text{K}$, for a $M = 15M_{\odot}$ model, over a range of solar to SMC-like metallicities (Ekström et al., 2012; Georgy et al., 2013).

For solar metallicity, observations in PerOB1 are in good agreement with the models (see Figure 9 in Gazak et al., 2014b). However, at SMC-like metallicity, the end-points of the models are systematically warmer than the observations. The temperature of the end-points of the evolutionary models of massive stars could depend on the choice of the convective mixing-length parameter (Schaller et al., 1992). That the models produce a higher temperature than observed could imply that the choice of a solar-like mixing-length parameter does not hold for

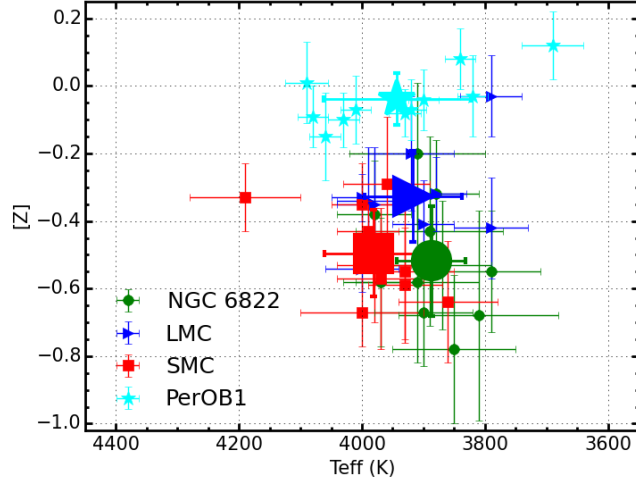


Figure 4.11 *Effective temperatures as a function of metallicity for four different data sets using the J-band analysis technique. There appears to be no significant variation in the temperatures of RSGs over a range of 0.55 dex. These results are compiled from the LMC, SMC (blue and red points respectively; ?), PerOB1 (a Galactic RSG cluster; cyan; Gazak et al., 2014b) and NGC 6822 (green). Mean values for each data set are shown as enlarged points in the same style and colour. The x-axis is reversed for comparison with Figure 4.12.*

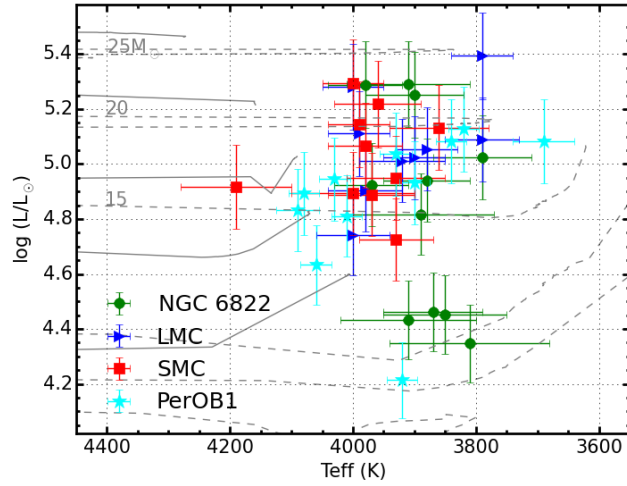


Figure 4.12 *H-R diagram for RSGs in PerOB1 (cyan), LMC (blue), SMC (red) and NGC 6822 (green) which have stellar parameters obtained using the J-band method. This figure shows that there appears to be no significant temperature differences between the four samples. Solid grey lines show SMC-like metallicity evolutionary models including rotation (Georgy et al., 2013). Dashed grey lines show solar metallicity evolutionary models including rotation (Ekström et al., 2012).*

higher-mass stars at lower metallicity.

Lastly, we note that the average spectral type of RSGs tends towards an earlier spectral type with decreasing metallicity over this range (Humphreys, 1979; Levesque & Massey, 2012). We argue that this is not in contradiction to the above results. Spectral types are derived for RSGs using the optical TiO band-heads at $\sim 0.65\mu\text{m}$, whereas in this study temperatures are derived using near-IR atomic features (as well as the line-free pseudo-continuum). The strengths of TiO bands are dependent upon metallicity which means that the spectral classification for RSGs at a constant temperature will differ (Davies et al., 2013a). Therefore, although historically spectral type has been used as a proxy for temperature, this assumption does not provide an accurate picture for RSGs.

4.5.3 AGB Contamination

As mentioned in Section 4.2.1, massive AGB stars are potential contaminants to our sample. These stars have similar properties to RSGs and can occupy similar mass ranges as lower-mass RSGs (Herwig, 2005), however, their lifetimes are around ~ 250 Myr (Doherty et al., 2010). Wood, Bessell & Fox (1983) argued for an AGB luminosity limit (due to the limit on the mass of the degenerate core) of $M_{bol} \sim -7.1$. Using this maximum luminosity, corrected for the distance to NGC 6822, yields $K = 14.0$. Four of our analysed stars have K -band magnitudes fainter than this limit, but excluding the results for these does not significantly alter any of our conclusions (and arguably, they would still be tracing the relatively young stellar population).

4.6 Conclusions

KMOS spectroscopy of red supergiant stars (RSGs) in NGC 6822 is presented. The data were telluric corrected in two different ways and the standard 3-arm telluric method is shown to work as effectively (in most cases) as the more time expensive 24-arm telluric method. Radial velocities of the targets are derived and are shown to be consistent with previous results in NGC 6822, confirming their extragalactic nature.

Stellar parameters are calculated for 11 RSGs using the J -band analysis method

outlined in Davies, Kudritzki & Figer (2010). The average metallicity within NGC 6822 is $\bar{Z} = -0.52 \pm 0.21$, consistent with previous abundance studies of young stars. We find an indication of a metallicity gradient within the central 1 kpc, however with a low significance caused by the small size and limited spatial extent of our RSG sample. To conclusively assess the presence of a metallicity gradient among the young population within NGC 6822 a larger systematic study of RSGs is needed.

The chemical abundances of the young and old stellar populations of NGC 6822 are well explained by a simple closed-box chemical evolution model. However, while an interesting result, we note that the closed-box model is unlikely to be a good assumption for this galaxy given its morphology.

The effective temperatures of RSGs in this study are compared to those of all RSGs analysed using the same method. Using results which span 0.55 dex in metallicity (solar to SMC) within four galaxies, we find no evidence for a systematic variation in average effective temperature with respect to metallicity. This is in contrast with evolutionary models which, for a similar change in metallicity, produces a shift in the temperature of RSGs of up to 450K. We argue that an observed shift in average spectral type of RSGs over this metallicity range does not imply a shift in average temperature.

These observations were taken as part of the KMOS Science Verification programme. With guaranteed time observations we have obtained data for RSGs in NGC 300 and NGC 55 at distances of ~ 1.9 Mpc, as well as observations of super-star clusters in M83 and the Antennae galaxy at 4.5 and 20 Mpc, respectively. Owing to the fact that RSGs dominate the light output from super-star clusters (Gazak et al., 2013) these clusters can be analysed in a similar manner (Gazak et al., 2014a), which will provide metallicity measurements at distances a factor of 10 larger than using individual RSGs! This work is the first step towards an ambitious proposal to survey a large number of galaxies in the Local Volume, motivated by the twin goals of investigating their abundance patterns, while also calibrating the relationship between galaxy mass and metallicity in the Local Group.

Bibliography

- Asplund M., Grevesse N., Sauval A. J., Scott P., 2009, ARA&A, 47, 481
- Battinelli P., Demers S., Kunkel W. E., 2006, A&A, 451, 99
- Bergemann M., Kudritzki R.-P., Plez B., Davies B., Lind K., Gazak Z., 2012, ApJ, 751, 156
- Bergemann M., Kudritzki R.-P., Würl M., Plez B., Davies B., Gazak Z., 2013, ApJ, 764, 115
- Bovy J., Rix H.-W., 2013, ApJ, 779, 115
- Cioni M.-R. L. et al., 2014, A&A, 562, A32
- Davies B., Kudritzki R.-P., Figer D. F., 2010, MNRAS, 407, 1203
- Davies B. et al., 2013a, ApJ, 767, 3
- Davies R. I. et al., 2013b, A&A, 558, A56
- de Blok W. J. G., Walter F., 2000, ApJ, 537, L95
- de Blok W. J. G., Walter F., 2003, MNRAS, 341, L39
- de Blok W. J. G., Walter F., 2006, AJ, 131, 343
- Demers S., Battinelli P., Kunkel W. E., 2006, ApJ, 636, L85
- Doherty C. L., Siess L., Lattanzio J. C., Gil-Pons P., 2010, MNRAS, 401, 1453
- Efremova B. V. et al., 2011, ApJ, 730, 88
- Ekström S. et al., 2012, A&A, 537, A146
- Evans C. J. et al., 2011, A&A, 527, A50

- Gazak J. Z., Bastian N., Kudritzki R.-P., Adamo A., Davies B., Plez B., Urbaneja M. A., 2013, MNRAS, 430, L35
- Gazak J. Z. et al., 2014a, ApJ, 787, 142
- Gazak J. Z., Davies B., Kudritzki R., Bergemann M., Plez B., 2014b, ApJ, 788, 58
- Georgy C. et al., 2013, A&A, 558, A103
- Gratier P., Braine J., Rodriguez-Fernandez N. J., Israel F. P., Schuster K. F., Brouillet N., Gardan E., 2010, A&A, 512, A68
- Gustafsson B., Edvardsson B., Eriksson K., Jørgensen U. G., Nordlund Å., Plez B., 2008, A&A, 486, 951
- Hernández-Martínez L., Peña M., Carigi L., García-Rojas J., 2009, A&A, 505, 1027
- Herwig F., 2005, ARA&A, 43, 435
- Houk N., Smith-Moore M., 1988, Michigan Catalogue of Two-dimensional Spectral Types for the HD Stars. Volume 4, Declinations -26° to -12° .
- Humphreys R. M., 1979, ApJ, 231, 384
- Huxor A. P., Ferguson A. M. N., Veljanoski J., Mackey A. D., Tanvir N. R., 2013, MNRAS, 429, 1039
- Hwang N., Lee M. G., Lee J. C., Park W.-K., Park H. S., Kim S. C., Park J.-H., 2011, ApJ, 738, 58
- Hwang N., Park H. S., Lee M. G., Lim S., Hodge P. W., Kim S. C., Miller B., Weisz D., 2014, ApJ, 783, 49
- Kirby E. N., Cohen J. G., Guhathakurta P., Cheng L., Bullock J. S., Gallazzi A., 2013, ApJ, 779, 102
- Komiyama Y. et al., 2003, ApJ, 590, L17
- Koribalski B. S. et al., 2004, AJ, 128, 16
- Lapenna E., Origlia L., Mucciarelli A., Lanzoni B., Ferraro F. R., Dalessandro E., Valenti E., Cirasuolo M., 2015, ApJ, 798, 23

- Lee H., Skillman E. D., Venn K. A., 2006, *ApJ*, 642, 813
- Letarte B., Demers S., Battinelli P., Kunkel W. E., 2002, *AJ*, 123, 832
- Levesque E. M., Massey P., 2012, *AJ*, 144, 2
- Massey P., Olsen K. A. G., Hodge P. W., Jacoby G. H., McNeill R. T., Smith R. C., Strong S. B., 2007, *AJ*, 133, 2393
- McConnachie A. W., 2012, *AJ*, 144, 4
- Muschielok B. et al., 1999, *A&A*, 352, L40
- Nieva M.-F., Przybilla N., 2012, *A&A*, 539, A143
- Nikolaev S., Weinberg M. D., 2000, *ApJ*, 542, 804
- Pagel B. E. J., Edmunds M. G., Smith G., 1980, *MNRAS*, 193, 219
- Richer M. G., McCall M. L., 1995, *ApJ*, 445, 642
- Schaller G., Schaerer D., Meynet G., Maeder A., 1992, *A&AS*, 96, 269
- Schlegel D. J., Finkbeiner D. P., Davis M., 1998, *ApJ*, 500, 525
- Sharples R. et al., 2013, *The Messenger*, 151, 21
- Sibbons L. F., Ryan S. G., Cioni M.-R. L., Irwin M., Napiwotzki R., 2012, *A&A*, 540, A135
- Tolstoy E., Irwin M. J., Cole A. A., Pasquini L., Gilmozzi R., Gallagher J. S., 2001, *MNRAS*, 327, 918
- Venn K. A. et al., 2001, *ApJ*, 547, 765
- Weisz D. R., Dolphin A. E., Skillman E. D., Holtzman J., Gilbert K. M., Dalcanton J. J., Williams B. F., 2014, *ApJ*, 789, 147
- Wolfire M. G., McKee C. F., Hollenbach D., Tielens A. G. G. M., 2003, *ApJ*, 587, 278
- Woo J., Courteau S., Dekel A., 2008, *MNRAS*, 390, 1453
- Wood P. R., Bessell M. S., Fox M. W., 1983, *ApJ*, 272, 99

Chapter 5

Red Supergiants in NGC 55

Observations – complete Data Reduction – undergoing
30% complete?

Appendix A

The First Appendix

Lorem ipsum dolor sit amet, consectetur adipiscing elit. Sed adipiscing porttitor turpis sed congue. Phasellus ac magna mi. Vivamus et dolor justo. Vivamus ligula dolor, consequat et sodales eget, mattis at ligula. Nulla arcu nisi, porttitor a ornare eget, luctus eget mi. Vivamus adipiscing turpis in ligula tempus blandit. Vestibulum rutrum sodales quam, quis blandit mauris sollicitudin in. Maecenas lacinia gravida velit nec venenatis. Curabitur eget orci aliquet augue adipiscing bibendum. Sed in tortor metus. Ut sit amet nisl odio. Maecenas accumsan, mauris a auctor egestas, nisl ante imperdiet arcu, ac volutpat erat neque rutrum turpis. Pellentesque ut est et lectus interdum fringilla sit amet non purus. Aliquam erat volutpat. Etiam rhoncus, leo vel facilisis lacinia, quam augue ultricies dui, nec feugiat nunc sapien quis diam.

Fusce vitae placerat purus. Sed porttitor, odio eu aliquam volutpat, arcu lectus vulputate nibh, non malesuada lectus arcu at enim. Sed arcu ante, faucibus eu pellentesque eu, ornare consequat nulla. Nunc consectetur, mauris vel elementum ullamcorper, nisi purus molestie mauris, quis lobortis libero orci id turpis. Duis sagittis nibh et nisl sagittis pulvinar. Ut imperdiet blandit feugiat. Etiam sit amet gravida sapien. Vestibulum dignissim eleifend aliquet. Suspendisse laoreet elementum massa, vitae pulvinar lorem viverra quis. Sed aliquet, erat eu aliquet ullamcorper, augue ligula bibendum ante, at euismod neque tellus eget elit. In congue, lorem eget consectetur bibendum, nibh est dignissim arcu, nec faucibus neque erat eu tellus. Nam ac augue purus.

Lorem ipsum dolor sit amet, consectetur adipiscing elit. Etiam ipsum sapien, blandit quis condimentum nec, blandit sed mauris. Nulla facilisi. Aliquam

pretium, est quis lobortis cursus, elit lorem pulvinar turpis, sed malesuada nulla magna at mi. Suspendisse potenti. Proin egestas turpis id nulla pretium elementum. Suspendisse potenti. Quisque vitae fermentum risus. Vivamus ut urna consectetur sem accumsan vestibulum eget ut augue. Vivamus facilisis posuere nunc, ut sagittis quam sodales ut. Donec ut nunc quis elit ultricies pulvinar. Vivamus varius elit quis libero semper molestie id ac ligula. Lorem ipsum dolor sit amet, consectetur adipiscing elit.

Quisque sit amet justo quis nibh elementum iaculis quis a dui. Vestibulum ante ipsum primis in faucibus orci luctus et ultrices posuere cubilia Curae; Maecenas nec egestas dolor. Nam massa erat, vulputate vel ultrices sit amet, aliquet vel massa. Nulla iaculis venenatis urna nec commodo. Fusce ac eros a arcu ullamcorper pharetra in non sapien. Vivamus tempor fermentum enim, eu consequat nibh porttitor sed. Quisque pellentesque eleifend felis, id dictum massa placerat fringilla. Mauris a dolor ipsum, at tincidunt arcu. Maecenas vitae massa arcu, sed commodo dui. Vestibulum aliquam ultrices odio, ut aliquet eros venenatis vel.

Morbi vestibulum massa eget risus lacinia id rhoncus elit feugiat. Vivamus venenatis, metus a elementum volutpat, neque nunc tempor felis, tristique sagittis nibh augue varius risus. Maecenas feugiat tincidunt sapien, et rutrum lorem tincidunt quis. Cum sociis natoque penatibus et magnis dis parturient montes, nascetur ridiculus mus. Proin eget nulla id felis cursus elementum vel quis lectus. Aenean posuere tortor eu ipsum interdum egestas. Vestibulum sed eros id enim tincidunt aliquet. Etiam eu rutrum quam. Phasellus commodo dolor vel eros laoreet tincidunt. Etiam interdum consectetur erat, in tempor lectus feugiat id.

Bibliography

- Asplund M., Grevesse N., Sauval A. J., Scott P., 2009, ARA&A, 47, 481
- Battinelli P., Demers S., Kunkel W. E., 2006, A&A, 451, 99
- Bergemann M., Kudritzki R.-P., Plez B., Davies B., Lind K., Gazak Z., 2012, ApJ, 751, 156
- Bergemann M., Kudritzki R.-P., Würl M., Plez B., Davies B., Gazak Z., 2013, ApJ, 764, 115
- Bovy J., Rix H.-W., 2013, ApJ, 779, 115
- Cioni M.-R. L. et al., 2014, A&A, 562, A32
- Davies B., Kudritzki R.-P., Figer D. F., 2010, MNRAS, 407, 1203
- Davies B. et al., 2013a, ApJ, 767, 3
- Davies R. I. et al., 2013b, A&A, 558, A56
- de Blok W. J. G., Walter F., 2000, ApJ, 537, L95
- de Blok W. J. G., Walter F., 2003, MNRAS, 341, L39
- de Blok W. J. G., Walter F., 2006, AJ, 131, 343
- Demers S., Battinelli P., Kunkel W. E., 2006, ApJ, 636, L85
- Doherty C. L., Siess L., Lattanzio J. C., Gil-Pons P., 2010, MNRAS, 401, 1453
- Efremova B. V. et al., 2011, ApJ, 730, 88
- Ekström S. et al., 2012, A&A, 537, A146
- Evans C. J. et al., 2011, A&A, 527, A50
- Gazak J. Z., Bastian N., Kudritzki R.-P., Adamo A., Davies B., Plez B., Urbaneja M. A., 2013, MNRAS, 430, L35
- Gazak J. Z. et al., 2014a, ApJ, 787, 142

- Gazak J. Z., Davies B., Kudritzki R., Bergemann M., Plez B., 2014b, ApJ, 788, 58
- Georgy C. et al., 2013, A&A, 558, A103
- Gratier P., Braine J., Rodriguez-Fernandez N. J., Israel F. P., Schuster K. F., Brouillet N., Gardan E., 2010, A&A, 512, A68
- Gustafsson B., Edvardsson B., Eriksson K., Jørgensen U. G., Nordlund Å., Plez B., 2008, A&A, 486, 951
- Hernández-Martínez L., Peña M., Carigi L., García-Rojas J., 2009, A&A, 505, 1027
- Herwig F., 2005, ARA&A, 43, 435
- Houk N., Smith-Moore M., 1988, Michigan Catalogue of Two-dimensional Spectral Types for the HD Stars. Volume 4, Declinations -26deg.0to -12deg.0.
- Humphreys R. M., 1979, ApJ, 231, 384
- Huxor A. P., Ferguson A. M. N., Veljanoski J., Mackey A. D., Tanvir N. R., 2013, MNRAS, 429, 1039
- Hwang N., Lee M. G., Lee J. C., Park W.-K., Park H. S., Kim S. C., Park J.-H., 2011, ApJ, 738, 58
- Hwang N., Park H. S., Lee M. G., Lim S., Hodge P. W., Kim S. C., Miller B., Weisz D., 2014, ApJ, 783, 49
- Kirby E. N., Cohen J. G., Guhathakurta P., Cheng L., Bullock J. S., Gallazzi A., 2013, ApJ, 779, 102
- Komiyama Y. et al., 2003, ApJ, 590, L17
- Koribalski B. S. et al., 2004, AJ, 128, 16
- Lapenna E., Origlia L., Mucciarelli A., Lanzoni B., Ferraro F. R., Dalessandro E., Valenti E., Cirasuolo M., 2015, ApJ, 798, 23
- Lee H., Skillman E. D., Venn K. A., 2006, ApJ, 642, 813
- Letarte B., Demers S., Battinelli P., Kunkel W. E., 2002, AJ, 123, 832
- Levesque E. M., Massey P., 2012, AJ, 144, 2
- Massey P., Olsen K. A. G., Hodge P. W., Jacoby G. H., McNeill R. T., Smith R. C., Strong S. B., 2007, AJ, 133, 2393
- McConnachie A. W., 2012, AJ, 144, 4
- Muschielok B. et al., 1999, A&A, 352, L40

- Nieva M.-F., Przybilla N., 2012, A&A, 539, A143
- Nikolaev S., Weinberg M. D., 2000, ApJ, 542, 804
- Pagel B. E. J., Edmunds M. G., Smith G., 1980, MNRAS, 193, 219
- Richer M. G., McCall M. L., 1995, ApJ, 445, 642
- Schaller G., Schaerer D., Meynet G., Maeder A., 1992, A&AS, 96, 269
- Schlegel D. J., Finkbeiner D. P., Davis M., 1998, ApJ, 500, 525
- Sharples R. et al., 2013, The Messenger, 151, 21
- Sibbons L. F., Ryan S. G., Cioni M.-R. L., Irwin M., Napiwotzki R., 2012, A&A, 540, A135
- Tolstoy E., Irwin M. J., Cole A. A., Pasquini L., Gilmozzi R., Gallagher J. S., 2001, MNRAS, 327, 918
- Venn K. A. et al., 2001, ApJ, 547, 765
- Weisz D. R., Dolphin A. E., Skillman E. D., Holtzman J., Gilbert K. M., Dalcanton J. J., Williams B. F., 2014, ApJ, 789, 147
- Wolfire M. G., McKee C. F., Hollenbach D., Tielens A. G. G. M., 2003, ApJ, 587, 278
- Woo J., Courteau S., Dekel A., 2008, MNRAS, 390, 1453
- Wood P. R., Bessell M. S., Fox M. W., 1983, ApJ, 272, 99